Forschungszentrum Karlsruhe
in der Helmholtz-Gemeinschaft

Wissenschaftliche Berichte
FZKA 6904

Inertialess Magnetohydrodynamic Flows in Expansions and Contractions

L. Bühler

Institut für Kern- und Energietechnik
Programm Kernfusion

Dezember 2003

Forschungszentrum Karlsruhe

in der Helmholtz-Gemeinschaft

Wissenschaftliche Berichte

FZKA 6904

Inertialess magnetohydrodynamic flows in expansions and contractions

L. Bühler

Institut für Kern- und Energietechnik
Programm Kernfusion

Forschungszentrum Karlsruhe GmbH, Karlsruhe
2003

Impressum der Print-Ausgabe:

Als Manuskript gedruckt

Forschungszentrum Karlsruhe GmbH
Postfach 3640, 76021 Karlsruhe

Mitglied der Hermann von Helmholtz-Gemeinschaft
Deutscher Forschungszentren (HGF)

ISSN 0947-8620

Inertialess magnetohydrodynamic flows in expansions and contractions

Abstract

Inductionless, incompressible MHD flows in expansions of rectangular ducts are investigated by asymptotic techniques for strong, uniform, externally applied magnetic fields. The geometries considered are closely related to applications in nuclear fusion reactors, where liquid alloys are used as breeding materials. The liquid metal velocities are very small so that inertia is negligible in comparison with the electromagnetic forces. The major balance of forces establishes in the core between pressure and Lorentz forces while viscous forces are confined to very thin boundary layers along the duct walls. Near the expansion one can observe an intense exchange of flow between the upstream and downstream cores with the corresponding side layers. This effect becomes more pronounced with decreasing length of the expansion region. For the limiting case of infinitesimally expansion length, i.e. for a sudden expansion an internal layer develops along magnetic field lines. This expansion layer matches the solutions in both rectangular ducts. Depending on the electric conductivity of the duct walls this layer is able to carry a significant amount of the total flow. The three-dimensional flow near the expansion drives additional electric currents which are responsible for higher pressure drop compared with fully developed conditions. As an example, the detailed flow structure in the expansion layer is analyzed and discussed for an expansion ratio of $4:1$.

Trägheitsfreie magnetohydrodynamische Strömungen in Expansionen und Kontraktionen

Zusammenfassung

Mittels asymptotischer Verfahren werden induktionsfreie, inkompressible magnetohydrodynamische Strömungen in Rechteckkanälen mit Querschnittserweiterungen untersucht, unter dem Einfluss starker, externer Magnetfelder. Ähnliche Geometrien findet man in Blankets von Fusionsreaktoren, in denen Flüssigmetalle als Brutmaterial verwendet werden. Die Geschwindigkeiten der flüssigen Metalle sind dabei sehr klein, so dass Trägheitskräfte im Vergleich zu den elektromagnetischen Kräften vernachlässigt werden. Im Kernbereich der Strömung stellt sich ein Gleichgewicht zwischen Druckkräften und Lorentzkräften ein. Viskose Kräfte beeinflussen die Strömung lediglich in dünnen Grenzschichten entlang der Kanalwände. Im Bereich der Expansion kommt es zu einem intensiven Austausch von Fluid zwischen den Kernströmungsgebieten und den Seitengrenzschichten. Mit abnehmender Länge der Expansion verstärken sich diese Effekte. Für den Grenzfall einer plötzlichen Querschnittserweiterung findet man schließlich eine interne Scherschicht, die sich entlang von magnetischen Feldlinien ausrichtet. Über diese Schicht werden die Lösungen in den beiden Rechteckkanälen kontinuierlich miteinander verbunden. Je nach elektrischer Leitfähigkeit der Kanalwände kann diese Schicht einen beachtlichen Teil des Volumenstroms aufnehmen. Im Bereich der Expansion treibt die dreidimensionale Strömung zusätzliche elektrische Ströme, die zu einem erhöhten Druckverlust führen. An einem Beispiel, für ein Expansionsverhältnis von $4:1$, wird die Struktur der Grenzschichtströmungen detailliert untersucht und diskutiert.

Inertialess magnetohydrodynamic flows in expansions and contractions

Contents

1 Introduction

In future nuclear fusion reactor blankets liquid metals such as Li or PbLi alloys serve as breeding material for generation of tritium which is one fuel component that does not occur naturally. A significant amount of the fusion power is released within the liquid metal and within the blanket structure. Any design concept which uses liquid metals additionally as coolant requires electrically insulating walls in order to minimize induced electric currents in the fluid when it moves at high speed through the strong magnetic field that is needed to confine the fusion plasma. Electrically insulating walls fabricated from silicon carbide composite materials are indeed considered in conceptional studies of highly advanced reactor models (Giancarli, Golfier, Nishio, Raffray, Wong and Yamada (2002)), but up to the present day, the technological feasibility of such designs remains to be proven. Near-term blanket research focusses therefore on more or less standard technologies where walls are fabricated from steel and no insulation on the wall is foreseen.

Liquid metal flows confined in conducting containers exert much stronger magnetohydrodynamic (MHD) interaction since currents and Lorentz forces are higher than in insulating ducts. For that reason the liquid metal can not be used as a coolant any more and a separate cooling system is required. The currently proposed designs consider walls which have internal cooling channels through which the electrically non-conducting coolant (helium at high pressure) removes the fusion heat at high speed. The liquid metal, however, is almost stagnant, but it circulates at very low velocity required for tritium extraction. Since the velocities are very small, inertia forces give only a minor fraction to the momentum balance.

The liquid metal is filled in gaps between cooling plates and the aspect ratio of the fluid regions, say the length measured along magnetic field lines / length perpendicular to the field is typically high. The fluid is distributed and collected to the breeding zone through a piping system which has much smaller dimensions. This means that at the entrance and at the exit the geometry expands and contracts preferentially in the direction of the magnetic field.

Expansions and contractions are important elements of actual fusion blankets but they are also basic geometric components of any liquid metal device. They received attention in the past by a number of authors and one should recall as examples the experiments reported by Branover, Vasil'ev and Gel'fgat (1967), Gel'fgat and Kit (1971) who consider inertial MHD flows in insulating sudden expansions, or Walker, Ludford and Hunt (1972), who study MHD flows through smoothly expanding insulating channels using an inertialess approximation. Smooth expansions with thin conducting walls had been considered by Walker (1981) or by Picologlou, Reed, Hua, Barleon, Kreuzinger and Walker (1989). The latter authors studied expansions and contractions of the type as shown in Fig. 1, where expansion and contraction regions are located periodically along the axis.

The present analysis considers MHD flows in a single expansion or contraction as shown in Fig. 1. The problem studied here corresponds in general to that treated by Walker (1981). While Walker introduces multiple layer techniques and calculates the flow in the inner (the viscous) and in the outer (inviscid) side layers, the numerical technique used here resolves the outer layers as a part of the core flow and treats the

inner layers in an integral manner. The length of the expansion section is chosen as a parameter. For various expansion lengths, fluid properties like pressure drop, flow rates in side layers, wall potentials, and core streamfunctions are calculated and compared. For the case of a sudden expansion an internal layer develops which is able to carry a considerable fraction of the total flow rate. The detailed structure of the flow in the internal layer is investigated.

In the analysis inertia effects are neglected. With this assumption the flow problem becomes linear so that the results obtained for an expansion flow apply as well for a flow in a contraction if the velocity is reversed. This assumption is fairly valid for smooth expansions in strong magnetic fields, when Lorentz forces are much stronger than inertia forces. But we should be aware of the fact that neglecting inertia at sudden expansions requires that the velocities are sufficiently small. Any engineering application in which a fluid is moving, however, has finite values of velocity and if inertia forces even if they may be very small. An experiment which is under current investigation in the MEKKA laboratory at the Forschungszentrum Karlsruhe will show at which values of velocity the inertialess approximation starts to be valid.

The present work deals with geometries which expand along magnetic field lines since this type of geometry is most closely related to application in fusion blankets. On the other hand the present geometry creates the strongest MHD interaction. Another possibility for plane expansions could be the expansion in the plane perpendicular to the field. Geometries of this kind have been investigated in the past and it was found that the additional pressure drop due to 3D flows near the expansions is negligible for large Hartmann numbers (see e.g. Molokov (1994)).

2 Formulation

2.1 Governing equations

Consider the magnetohydrodynamic flow, governed by the balance of momentum

$$\frac{1}{N}\left[\partial_t \mathbf{v} + (\mathbf{v}\cdot\nabla)\,\mathbf{v}\right] = -\nabla p + \frac{1}{Ha^2}\nabla^2\mathbf{v} + \mathbf{j}\times\mathbf{B} \tag{1}$$

and mass conservation

$$\nabla\cdot\mathbf{v} = 0, \tag{2}$$

and by Ohm's law

$$\mathbf{j} = -\nabla\phi + \mathbf{v}\times\mathbf{B} \tag{3}$$

with

$$\nabla\cdot\mathbf{j} = 0. \tag{4}$$

In the equations shown above $\mathbf{v}$, $\mathbf{B}$, $\mathbf{j}$, p, ϕ stand for velocity, magnetic induction, current density, pressure and electric potential, scaled by the reference quantities v_0, B_0, $j_0 = \sigma v_0 B_0$, $\sigma v_0 B_0^2 L$ and $v_0 B_0 L$, respectively. The scale of velocity v_0 may be chosen as the average velocity in a particular cross section of the duct where L is a typical length scale. The quantity B_0 is the magnitude of the applied magnetic induction. The fluid properties like the electric conductivity σ, the kinematic viscosity ν, and the density ρ, are assumed to be constant.

The flow is governed by two nondimensional parameters, the Hartmann number Ha and the interaction parameter N

$$Ha = B_0 L\sqrt{\frac{\sigma}{\rho\nu}}\,, \quad N = \frac{\sigma L B_0^2}{\rho v_0}\,. \tag{5}$$

The square of the Hartmann number characterizes the ratio of electromagnetic forces to viscous forces while the interaction parameter represents the ratio of electromagnetic forces to inertia forces.

At the fluid wall interface the flow satisfies the no-slip condition

$$\mathbf{v} = 0, \tag{6}$$

and continuity of electric potential (no contact resistance)

$$\phi = \phi_w. \tag{7}$$

The walls of the duct are thin and electrically conducting so that the thin wall condition (compare Walker (1981)) applies for the determination of the wall potential ϕ_w as

$$\mathbf{j}\cdot\mathbf{n} = \nabla\cdot\left(c\nabla_t\phi_w\right). \tag{8}$$

Here ∇_t denotes the components of the gradient operator in directions tangential to the wall and c stands for the wall conductance ratio

$$c = \frac{\sigma_w t_w}{\sigma L}. \tag{9}$$

It describes the conductivity of the wall with thickness t_w compared with the conductivity of the fluid.

2.2 Core solution

For many applications in fusion the interaction parameter is very high so that inertia terms are negligible. In the following analysis we suppose that the magnetic field is uniform, and we chose the coordinate system in such a way that $\mathbf{B} = \hat{\mathbf{z}}$. The electromagnetic force or Lorentz force then becomes $\mathbf{j} \times \mathbf{B} = j_y\hat{\mathbf{x}} - j_x\hat{\mathbf{y}}$ and the induced electric field is $\mathbf{v} \times \mathbf{B} = v\hat{\mathbf{x}} - u\hat{\mathbf{y}}$. In this frame of reference the three components of the momentum equation read in the inertialess limit for $N \to \infty$ as

$$\begin{aligned} \partial_x p \quad - j_y \quad &= \tfrac{1}{Ha^2}\nabla^2 u, \\ \partial_y p \quad + j_x \quad &= \tfrac{1}{Ha^2}\nabla^2 v, \\ \partial_z p \qquad\quad &= \tfrac{1}{Ha^2}\nabla^2 w, \end{aligned} \tag{10}$$

and Ohm's law becomes

$$\begin{aligned} -\partial_x \phi \quad + v \quad &= j_x, \\ -\partial_y \phi \quad - u \quad &= j_y, \\ -\partial_z \phi \qquad\quad &= j_z. \end{aligned} \tag{11}$$

Conservation of mass and charge read as

$$\partial_x u + \partial_y v + \partial_z w = 0, \tag{12}$$

$$\partial_x j_x + \partial_y j_y + \partial_z j_z = 0. \tag{13}$$

The kinematic and electric boundary conditions remain as shown in equations (6) - (**??**).

It is possible to reduce the number of unknowns in the basic equations (10)-(13) by eliminating currents and velocity and to derive decoupled equations for potential and for pressure. To proceed in this direction we take the x and y component of the momentum equation (10) and eliminate pressure by differentiation with respect to y and x, respectively. This yields

$$-\partial_y j_y - \partial_x j_x = \partial_z j_z = \frac{1}{Ha^2}\nabla^2 \left(\partial_y u - \partial_x v\right). \tag{14}$$

Application of charge conservation (13) in Ohm's law (11) leads to

$$\partial_y u - \partial_x v = -\nabla^2 \phi, \tag{15}$$

so that we find from (14) with $\partial_z j_z = -\partial_{zz}\phi$ the equation governing potential as

$$\frac{1}{Ha^2}\nabla^4 \phi = \partial_{zz}\phi. \tag{16}$$

As for potential it is possible to derive an equation governing the pressure distribution. By applying the divergence operator on (10) using mass conservation we find

$$\nabla^2 p = \partial_z w. \tag{17}$$

After applying the operator ∇^2 we recover

$$\nabla^4 p = \partial_z \nabla^2 w \tag{18}$$

and using the $z-$ component of (10) we find

$$\frac{1}{Ha^2}\nabla^4 p = \partial_{zz} p. \tag{19}$$

We may also derive an equation governing the component of velocity w. Differentiation of (17) with respect to z and use of the z component of (10) yields

$$\frac{1}{Ha^2}\nabla^4 w = \partial_{zz} w. \tag{20}$$

Equations (16), (19), and (20) are exact in the inertialess limit. These equations are later used to reconstruct viscous solutions in thin boundary layers.

For high Hartmann numbers the flow is mainly governed by a balance between pressure forces and Lorentz forces while viscous forces are negligible compared with Lorentz forces in the so-called cores. Viscous forces are important only in thin boundary layers along walls or within viscous internal layers which spread along magnetic field lines into the fluid from discontinuities at the wall. Layers in which the magnetic field has a normal component are known as the Hartmann layers and layers which are aligned with the magnetic field are called the parallel layers.

The coordinate system introduced above applies well for the description of the flow in all layers which occur in the present expansion problem, since in each layer always one pair of coordinates is oriented tangential to the layer while the other coordinate is perpendicular to the layer. For that reason the equations derived above may serve as a basis for the boundary layer analysis which forms a main part of the present report. The flow outside the layers is calculated using a numerical code based on asymptotic techniques that is able to solve the MHD equations in an almost arbitrary domain. The code uses a coordinate system that differs from the one introduced above. In the numerical code two coordinates are boundary-fitted while the third direction coincides with the direction of the applied magnetic field, i.e. with $\hat{\mathbf{z}}$. A brief description of the code and a number of application examples has been published by Bühler (1995). The special coordinate system used in the numerical calculation becomes singular in the sense that the unit volume vanishes if one wall is perfectly aligned with the magnetic field. For that reason the code is not able to deal directly with walls which are perfectly aligned with the magnetic field. Such walls are for example the side walls of the rectangular channels. Bühler (1995) already showed that slight "elliptical" deformations of the side walls remove this mathematical difficulty and yield in the limit (for vanishing deviation from a straight line) the exact solution for rectangular duct flow in case of well conducting walls.

Although we shall not describe all mathematical details of the numerical procedure in detail here, we outline some specific properties of the flow which are required later for a reconstruction of the solution in the viscous layers. Let us consider the equations (10) in the inviscid limit as $Ha \to \infty$. It follows then immediately that

- the core pressure (subscript c indicates values in the core) is uniform along magnetic field lines, i.e.

$$\partial_z p_c = 0. \tag{21}$$

We find from (16) in the inviscid limit as $Ha \to \infty$ that $\partial_{zz}\phi = 0$. The potential varies linearly along magnetic field lines. For any $z-$symmetric problem (as the present one) symmetry requires that $\phi(z) = \phi(-z)$ so that

- the core potential is uniform along magnetic field lines,

$$\phi_c \neq \phi(z). \tag{22}$$

It can be shown that the conditions (21) and (22) are even valid with sufficient accuracy within the viscous Hartmann layers. The error in p and ϕ introduced by the approximation within the viscous layer is of the order $O(Ha^{-2})$ if the magnetic field is perpendicular to the wall (Moreau (1990)) or $O(Ha^{-1})$ if the magnetic field has a normal and a tangential component to the wall.

Since p_c and ϕ_c do not vary along field lines it follows directly from Ohm's law (11) that

- the core velocity transverse to the field is uniform along magnetic field lines,

$$u_c \neq u(z), \quad v_c \neq v(z). \tag{23}$$

In the following we consider geometries which expand in the direction of the magnetic field along a finite expansion length L_{exp}. A sketch of such a geometry is shown in Fig. 1. The geometry is built by two semi-infinite rectangular ducts. Both extend in the direction transverse to the magnetic field from $-1 < y < 1$. Along field lines the geometry extends from $-Z < z < Z$, where $Z = Z(x)$. The walls at $y = \pm 1$ are called the side walls and the walls at $z = \pm Z$ are called the Hartmann walls. The large duct has a square cross section with Hartmann walls at $z = \pm Z_C = \pm 1$, while the Hartmann walls of the smaller duct are at $z = \pm Z_c$. The quantity Z_C/Z_c may be called the expansion ratio.

In a parametric study we reduce L_{exp} gradually. By this procedure we obtain data for a whole family of expansions and find in the limit of infinitesimal L_{exp} the result for a sudden expansion. A similar approach had been used successfully to model the flow in a U$-$bend by Molokov and Bühler (1994) in order to circumvent the singularity that would arise in case of walls exactly aligned with the magnetic field.

A geometry with sharp corners at $x = \pm\frac{1}{2}L_{\text{exp}}$ as shown in Fig. 1 leads to the formation of three cores. One is located in the small duct for $x < -\frac{1}{2}L_{\text{exp}}$, one is within the expansion for $-\frac{1}{2}L < x < \frac{1}{2}L_{\text{exp}}$, and the third one forms in the large duct for $x > \frac{1}{2}L_{\text{exp}}$. The cores are separated from each other by two internal layers called the Ludford layers. These layers spread from the corners at $x = \pm\frac{1}{2}L_{\text{exp}}$ into the fluid along magnetic field lines. The existence of such layers and their characteristic features for 2D expansions has been shown by Hunt and Leibovich (1967). The z- components of velocity varies within the Ludford layers in such a way that the values of both cores are

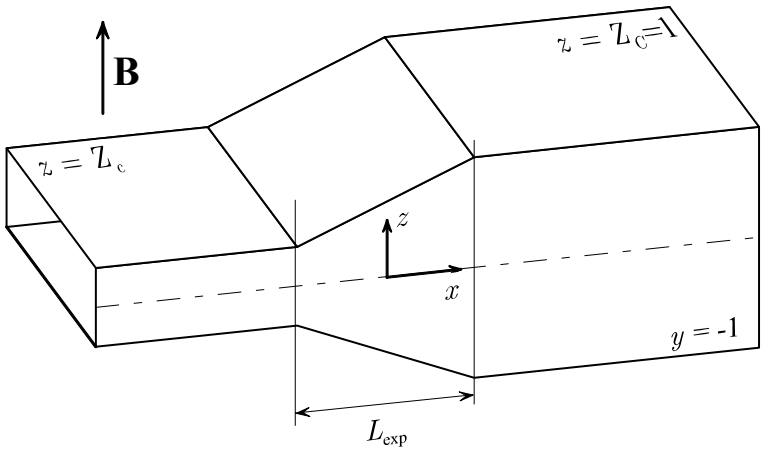

Figure 1: Sketch of an expansion

approached asymptotically towards both sides of the layer. A typical thickness of the Ludford layers is for inertialess flows $\delta_L \sim Ha^{-1/2}$. For very short expansions, say for L_{exp} on the order of δ_L both Ludford layers merge with the intermediate core and form a single expansion layer of thickness $\delta_e \sim Ha^{-1/2}$.

If the corners at $x = \pm\frac{1}{2}L_{\text{exp}}$ are made smooth we do not find any Ludford layer and the solution exhibits only one single core. Nevertheless, the solution for velocity varies on a typical geometric scale L_{exp} and we recover the expansion layer again as $L_{\text{exp}} < Ha^{-1/2}$.

3 Results for high Hartmann numbers

We discuss in the following results for flows at high Hartmann numbers, i.e. for $Ha \gg c^{-1/2}$. For these conditions the flow in the core but also the mass fluxes carried by parallel layers become independent of the Hartmann number and the fluid flows in the core as being inviscid. With this assumption the currents carried by the viscous layers tangential to the walls become negligible in comparison with the currents carried inside the wall, so that the solution of the problem in the cores becomes independent of the viscous details in the layers. This allows us to determine a core solution a priory without knowing details of the viscous flow in the layers. In a separate section below we shall reconstruct details of the viscous flow in the boundary and internal layers. The wall conductance ratio used in the present calculations is $c = 0.05$.

Let us consider flows through an expansion located between two semi-infinite rectangular ducts. In the expansion region the upper Hartmann wall is placed at $Z(x) = Z_c + \frac{1}{2}(Z_C - Z_c)\left(1 + \sin\frac{\pi x}{L_{\rm exp}}\right)$ and we chose an expansion ratio of 4 with $Z_C = 1,\ Z_c = 0.25$. The family of expansions depends on the length of the expansion section $L_{\rm exp}$. Several contours for different $L_{\rm exp}$ are shown in Fig. 2.

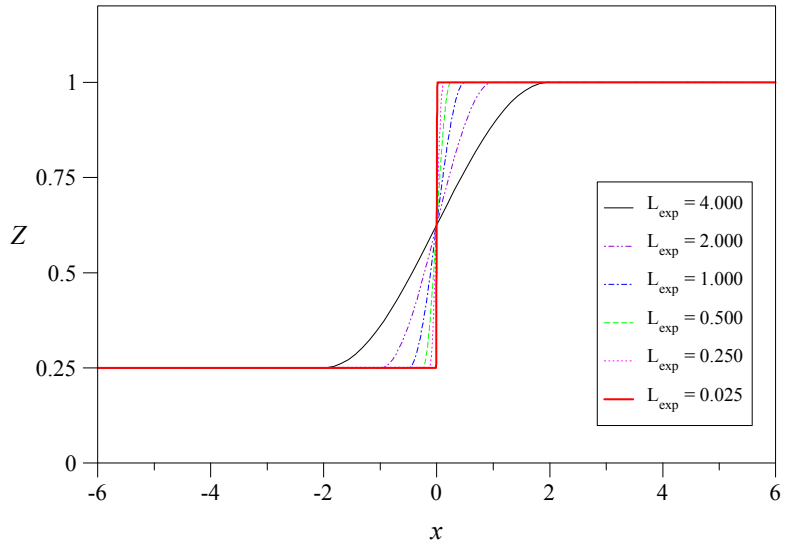

Figure 2: Contours of expansions for different $L_{\rm exp}$

The variation of pressure along the axis of the pipe is shown in Fig. 3. We observe the fully established MHD flow with uniform pressure gradients in both the large and the small duct at some distance from the expansion region. Fully developed conditions in ducts with $c \gg Ha^{-1/2}$ establish flow rates q_c and q_s, in the core and in the side layers, according to Tillack and McCarthy (1989). In the present notation these flow rates read as

$$q_c = -\left(1 + c^{-1}Z\right) Z\, \partial_x p, \quad q_s = -\frac{1}{3c} Z^3 \partial_x p. \tag{24}$$

In accordance with the velocity scale introduced at the beginning, where v_0 was the average velocity in the reference cross section, the total flow carried in a quarter of the

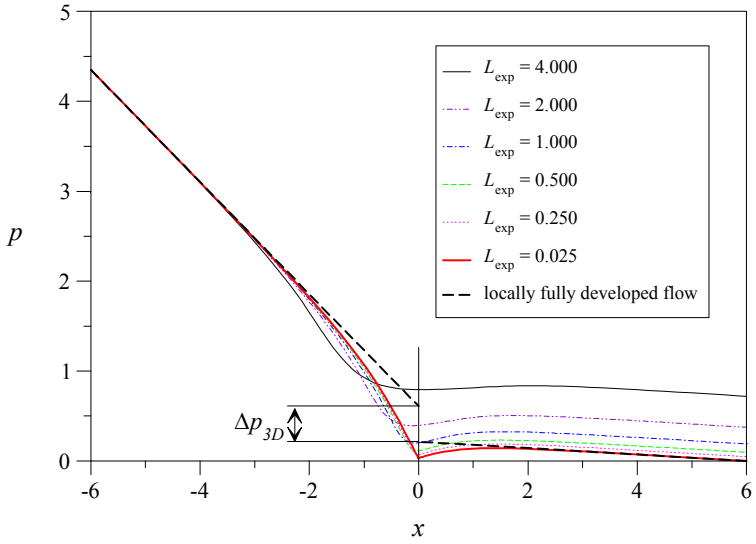

Figure 3: Pressure along the axis for different L_{exp} and $c = 0.05$, $Ha = \infty$

duct is

$$q = q_c + q_s = 1. \tag{25}$$

Therefore, the fully developed flow in a rectangular duct with vertical extension Z has a pressure gradient according to

$$\partial_x p = -\frac{1}{Z}\frac{\frac{c}{Z}}{1 + \frac{c}{Z} + \frac{1}{3}Z}. \tag{26}$$

Both fully developed pressure gradients in the small and the large duct are indicated in Fig. 3. It can be seen that the computational domain is sufficiently long that the flow can reach fully established conditions at the entrance and at the exit (see also Fig. 4). The parametric study for the influence of different L_{exp} shows, as expected, the smallest pressure drop in case of long expansions. The total pressure drop increases as the expansion length decreases, say when we approach the geometry of a sudden expansion.

The pressure gradients along the axis are shown in Fig. 4. The analytically known fully established conditions are approached perfectly after some distance (three characteristic lengths) upstream and downstream from the expansion region. The solutions exhibit a stronger pressure gradient when approaching the expansion. Within the expansion the magnitude of pressure gradient increases and we observe near the end of the expansion and in the square duct a partial pressure recovery.

The parametric study shows further that the solution for pressure gradient develops a singularity near $x = 0$ if L_{exp} becomes very small. The pressure gradient becomes discontinuous with a finite jump at $x = 0$ for infinitesimally small L_{exp}. Figure 5 summarizes these results and shows clearly the different values of pressure gradient at $x = -0$ and $x = +0$ for a sudden expansion. Associated with a discontinuous pressure gradient is a discontinuity in transverse current density and velocity. Such non-physical discontinuities are a direct consequence of neglecting viscosity within the expansion

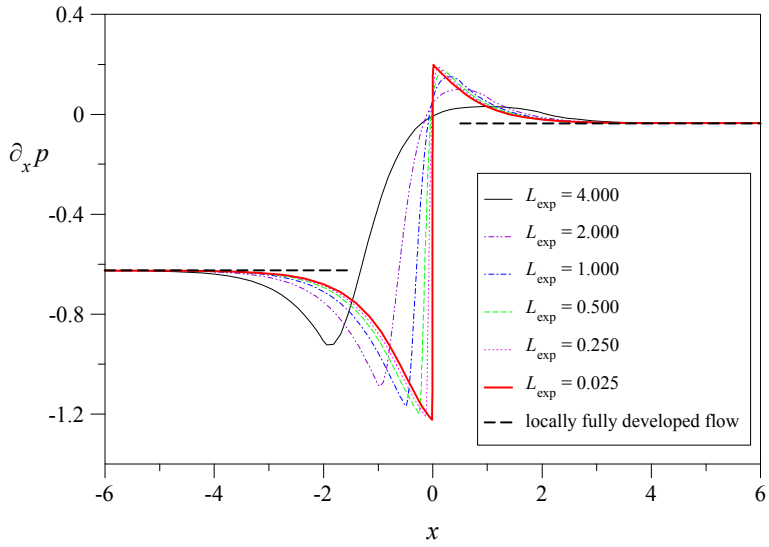

Figure 4: Axial component of pressure gradient along the axis for different L_{exp} and $c = 0.05$, $Ha = \infty$

layer. The viscous expansion layer becomes important for short expansion lengths, i.e. for $L_{\text{exp}} \lesssim O\left(Ha^{-1/2}\right)$. A viscous solution within the expansion layer will smoothly match the solutions in both cores near $x = 0$. This point is discussed later in more detail. An explanation for the phenomena observed above, especially for the pressure recovery in inertialess flows, may be obtained by considering Fig. 6. In the small duct for $x < 0$ the average velocity is higher than the velocity in the large duct for $x > 1$ due to the difference in cross sections. As a result the induced potential $\mathbf{v} \times \mathbf{B}$ in fully established flow is higher for the small duct, indicated in the figure as $\oplus\oplus\oplus$ and $\ominus\ominus\ominus$ in comparison with the smaller values in the large duct indicated by $\oplus$ and $\ominus$. As a consequence there exists an axial potential difference that drives electric currents along the walls (inside the wall, but also in the fluid). Axial currents are present only for 3D flows and these currents are therefore called the 3D currents. 3D currents require closure of the circuit through the fluid at $x < 0$ and $x > 0$ as shown in the sketch. In these regions the 3D currents have a y component and thus cause additional Lorentz forces which oppose the flow for $x < 0$ but accelerate the flow for $x > 0$. In the small duct part of the mechanical energy is converted into electric energy. This energy extraction from the flow results in higher pressure drop in front of the expansion. A significant part of the electric energy is irreversibly dissipated by Ohmic heating but a considerable fraction is reconverted into mechanical energy for $x > 0$ as can be observed from reversed pressure gradients in Fig. 4. For very long expansions the current circuit is long and the corresponding electric resistance is high. For such conditions the additional currents and associated effects on pressure drop and flow distribution remain small. The highest 3D currents are possible for a sudden expansion for which the Ohmic heating and total pressure drop reaches maximum values.

As a consequence of the strong braking of the flow by 3D currents for $x < 0$ the fluid tries to bypass the core. For that reason there occurs an exchange of mass between

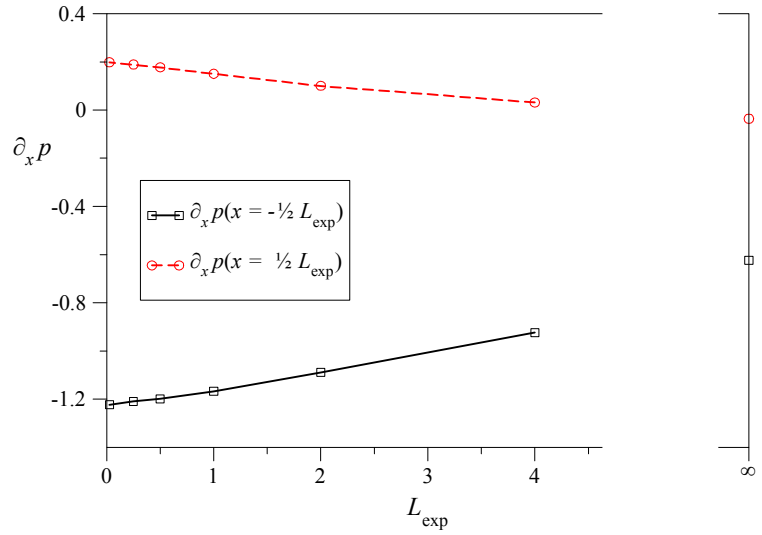

Figure 5: Pressure gradient on the axis at the beginning and at the end of the expansion region for different $L_{\text{exp}}$and $c = 0.05$, $Ha = \infty$

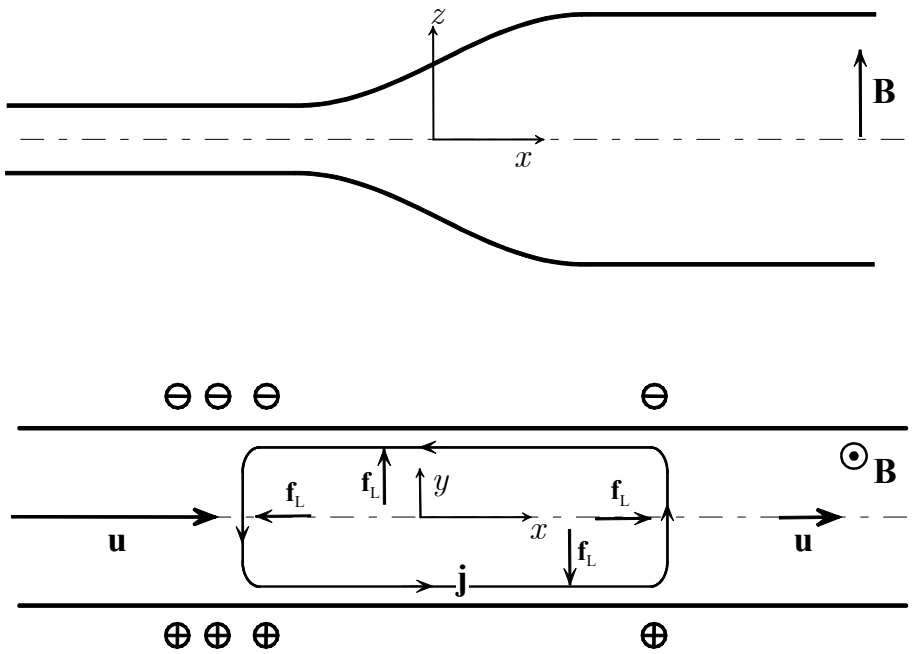

Figure 6: Sketch for explaining 3D effects in expanding MHD flows

the core and the side layers. These observations may be clarified by projecting the core mass flux in form of isolines of a 2D streamfunction onto a plane which is perpendicular to the applied magnetic field. The streamfunction is defined as

$$\psi(x,y) = -\int_0^y \int_0^Z u\, dz\, dy \tag{27}$$

and core streamlines (isolines of ψ) are shown in Fig. 7 for the whole family of expansions investigated. The horizontal components of core velocity are related with ψ as

$$u_c = -\frac{1}{Z}\partial_y \psi, \quad v_c = \frac{1}{Z}\partial_x \psi. \tag{28}$$

The fluid which leaves or enters the core at the sides is collected and redistributed in the side layers at $y = \pm 1$. The exchange of mass is favoured in addition by the Lorentz forces near the sides created by the 3D currents (compare Fig 6). These forces push the fluid towards the side walls and support actively the exchange of mass between core and side layers. The regions over which the ducts expand are indicated in Fig 7. We observe how the exchange of mass with the sides becomes intensified as $L_{\rm exp}$ decreases. For very short expansions, as $L_{\rm exp} \to 0$, the singular behavior becomes visible in the sense that a thin expansion layer forms at $x = 0$ which is fed by the core flow at the upstream side at $x < 0$. Only a small fraction of the flow crosses the expansion layer. The major part is carried within the layer towards the sides where it creates a discontinuity in the side layer mass flux.

Figure 8 shows the fraction of flow which is carried by the side layers. Far upstream and downstream we recover the side layer flow rate of a fully established MHD flow in conducting ducts. The fraction of flow carried by the side layers for fully developed conditions becomes with (24) and (26)

$$q_s = \frac{\frac{1}{3}Z}{1 + \frac{c}{Z} + \frac{1}{3}Z}. \tag{29}$$

A comparison of the numerically obtained values with the latter formula shows errors which are smaller than 2×10^{-4} for the discretization used. Approaching the expansion, the side layer flux increases continuously due to the braking of the core flow in front of the expansion. Within the expansion region the side layer flux increases further to reach a maximum value before is decreases downstream in order to approach the fully established condition. As discussed already above, 3D effects become more significant for shorter expansion lengths $L_{\rm exp}$. In the limit of a sudden expansion, when $L_{\rm exp} \to 0$, the side layer flow rate becomes discontinuous at $x = 0$. The discontinuity is caused by the flow that is supplied to the side layer by the expansion layer located at $x = 0$. Immediately behind the expansion nearly 80% of the flow is carried by the side layer. This flow rate is later on monotonically reduced to about 24.5% which is the known value corresponding to a fully developed flow in electrically conducting square ducts according to (29). The side layer flow rates immediately in front and behind the expansion are shown in Fig. 9 to demonstrate the singular behavior as $L_{\rm exp} \to 0$.

The flow quantities discussed above, especially the flow rates carried by the side layers are difficult to determine experimentally. However, since flow rates are directly

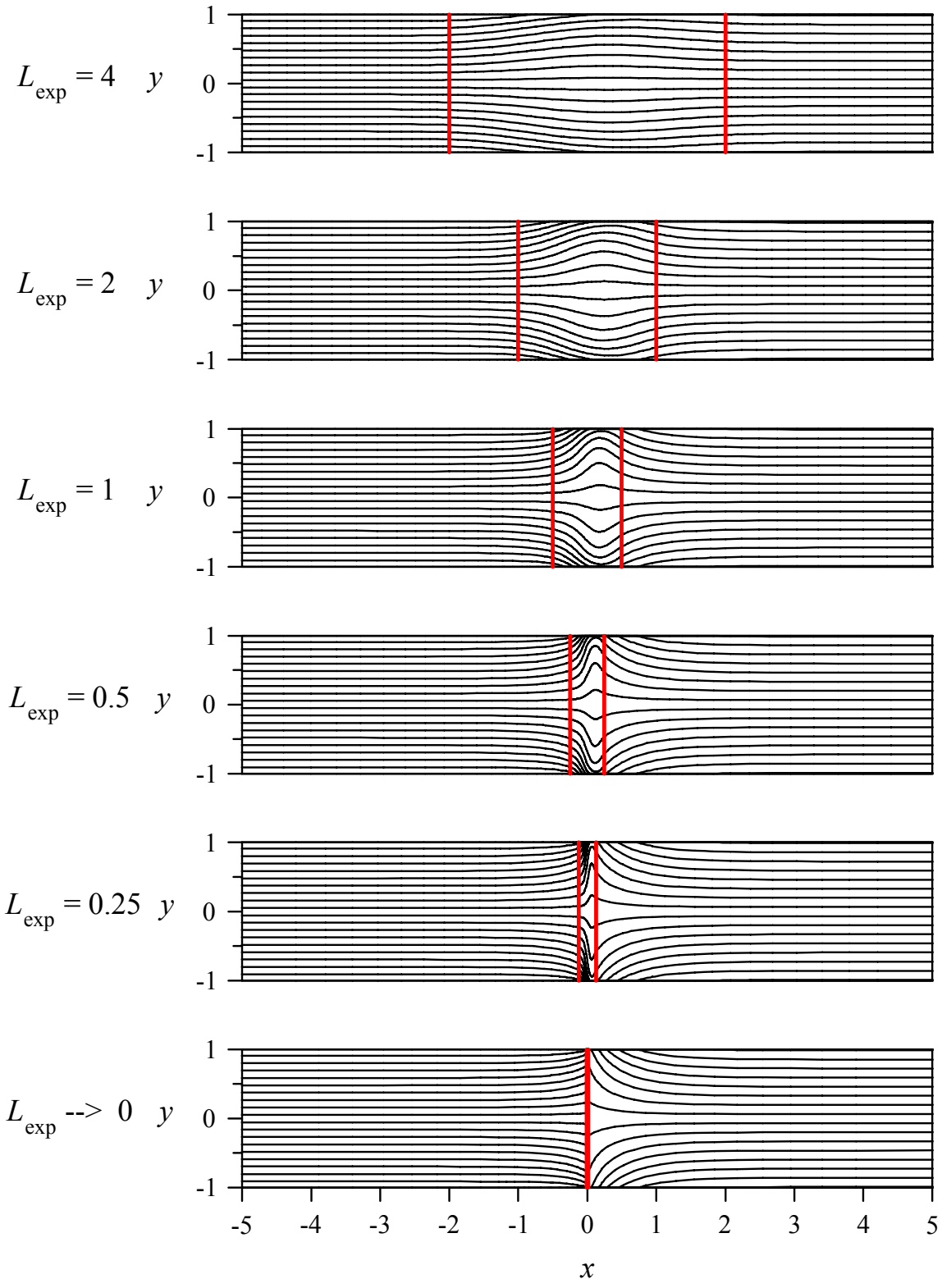

Figure 7: Streamlines for different lengths L_{exp} of the expanding section

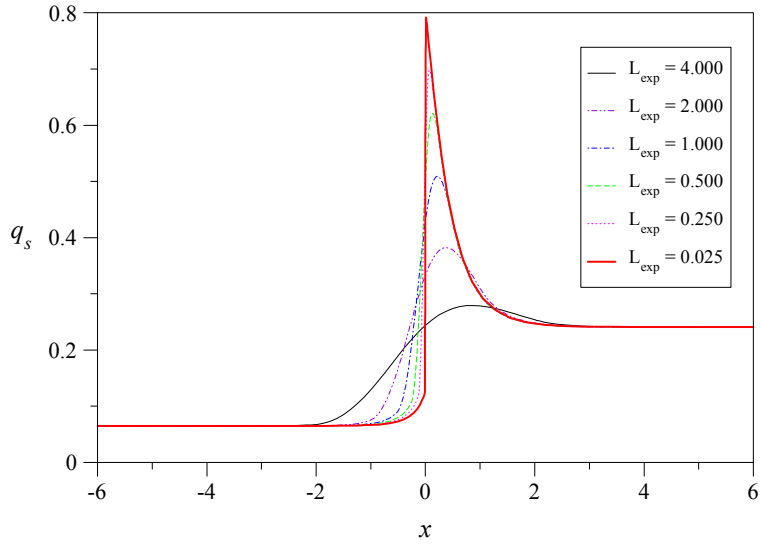

Figure 8: Fraction q_s of flow carried by the side layer

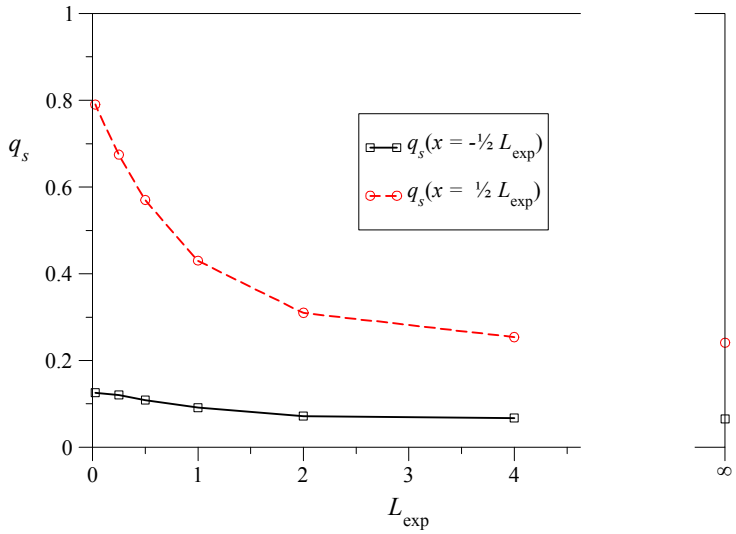

Figure 9: Side layer flow rate q_s at the beginning and at the end of the expansion region for different L_{exp} and $c = 0.05$, $Ha = \infty$

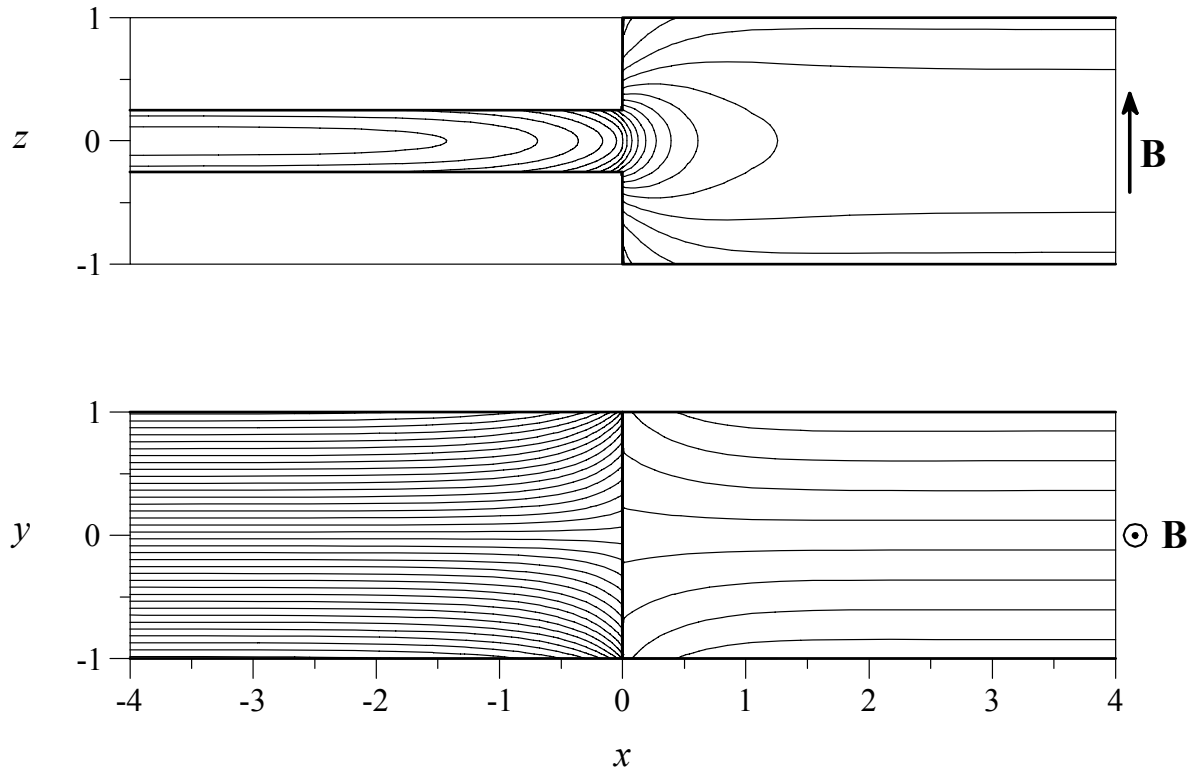

Figure 10: Isolines of wall potential on the side wall and on the top or the bottom wall. The potential difference between two isolines is 0.175

related to wall potentials it is useful to display this information in Fig.10. The figure shows isolines of wall potential on the side wall and on the top or the bottom wall. A comparison with the core streamfunction plotted in Fig. 7 shows that the potential on the Hartmann wall may serve, after appropriate scaling (different scales in small and large duct), as an approximate streamfunction for visualizing the core flow. This means that potential measurements which are taken at the Hartmann wall measure directly flow properties like streamfunction or velocity. The reason becomes obvious if we consider Ohm's law (11). Both variables, velocity and potential are of the order unity while currents are as small as the order of c in fully developed flows or of the order $c^{1/2}$ in 3D flows (Walker (1986)). Neglecting the currents yields

$$u \approx -\partial_y \phi, \quad v \approx \partial_x \phi \tag{30}$$

and we see by comparison with (28) that $\psi \approx Z\phi$ in the large and in the small duct.

So far we considered integral properties of the flow. Details such as velocity profiles in the side layers or velocity profiles in the expansion layer will be addressed in the next sections in which asymptotic techniques are used to reconstruct the flow in those layers.

4 Viscous layers

We derived above inviscid solutions which are valid almost everywhere in the fluid region but require modification in viscous boundary and internal layers. These layers are the Hartmann layers, the side layers and the internal layers if present. We start the analysis here for the simplest case of a Hartmann layer. In a second step we consider the side layers and finally for the example of a sudden expansion we investigate flow properties in the expansion layer.

4.1 Hartmann layers

Hartmann layers occur at walls at which the magnetic field has a normal component. As already mentioned, p and ϕ are constant across the Hartmann layers up to the the order $O\left(Ha^{-2}\right)$ if the magnetic field is perpendicular to the wall (Moreau (1990)) or $O\left(Ha^{-1}\right)$ if the magnetic field has a normal and a tangential component to the wall. It is further known that the velocity components tangential to the wall exhibit an exponential decay towards the wall in order to satisfy the no-slip condition at the wall. The velocity in the layer is

$$\mathbf{v} = \mathbf{v}_c \left(1 - \exp\left(-n\right)\right), \tag{31}$$

where $\mathbf{v}_c$ is the inviscid or core solution. The variable n is the local wall normal coordinate along the inward unit normal $\mathbf{n}$, scaled by the local thickness of the Hartmann layer which is $\delta_h = \left(Ha\,\hat{\mathbf{z}} \cdot \mathbf{n}\right)^{-1}$. All these properties are already implemented in the numerical method used here and need not to be discussed in more detail. For further information about the treatment of Hartmann layers in the code see Bühler (1995).

4.2 Side layers

At walls which are exactly aligned with the magnetic field we find a second type of boundary layers. The numerical code used here takes this layer into account in the sense that its integral properties are preserved. Especially the high mass flux carried by the layer and the electric potential at the side wall is calculated precisely if the conductivity of the side wall is much higher than the conductivity of the parallel layer, when $c \gg Ha^{-1/2}$. The velocity in the layer, however, has to be reconstructed in a subsequent step from the integral quantities via a boundary layer analysis.

Let us suppose that an inviscid solution to the problem is known. We know core potentials and velocities close to the side walls. Then we are able to derive asymptotic equations which govern the viscous flow in the side layer. For this purpose we introduce a stretched coordinate in (16) say in the layer at $y = -1$ such that

$$y + 1 = \delta_s \eta, \tag{32}$$

where δ_s stands for the thickness of the side layer (see Fig. 11). A reasonable balance of viscous and Lorentz forces requires that $\delta_s = Ha^{-1/2}$ and we find at leading order of the analysis the equation governing the potential in the side layer,

$$\partial_\eta^4 \phi = \partial_{zz} \phi. \tag{33}$$

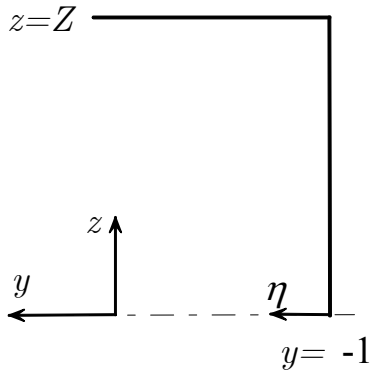

Figure 11: Stretched coordinates in the side layer at $y = -1$

The velocity in the layer is related at this order of approximation to the potential as

$$u = -Ha^{1/2}\partial_\eta \phi. \tag{34}$$

It has been shown by Walker (1981) that the thin wall condition (**??**) at Hartmann walls, formulated in stretched coordinates results in a uniform potential along the stretched direction, i.e. the wall acts as a perfect conductor in this direction if $c\,Ha \gg 1$, if the wall is better conducting than the Hartmann layer. For that reason the potential equals the core potential at the Hartmann wall and the viscous correction vanishes at $z = \pm Z$. As $\eta \to \infty$ the solution must match the core solution which is equivalent with the requirement that viscous corrections to the core potential and velocity vanish. In addition the velocity must vanish along the side wall and the potential equals that of the side wall at $\eta = 0$.

We decompose the potential as $\phi = \phi_c + \phi_s$, into an inviscid core solution ϕ_c and into a viscous side layer correction ϕ_s. Similarly we decompose the velocity as $u = u_c + u_s$, where u_c and u_s stand for the core velocity and the viscous correction in the side layer.

Equation (33) has the z- symmetric solution that does not grow indefinitely as $\eta \to \infty$:

$$\phi_s = \sum_{k=0}^{\infty} (a_k \cos \alpha_k \eta + b_k \sin \alpha_k \eta) \exp \alpha_k \eta \, \cos \beta_k z, \tag{35}$$

where

$$\beta_k = \frac{2k+1}{2}\frac{\pi}{Z}, \quad \alpha_k = -\sqrt{\beta_k/2}. \tag{36}$$

The velocity evaluates as

$$u_s = -Ha^{1/2}\partial_\eta \phi_s = \tag{37}$$

$$-\sum Ha^{1/2}\alpha_k \left[(b_k + a_k)\cos \alpha_k \eta + (b_k - a_k)\sin \alpha_k \eta\right] \exp \alpha_k \eta \, \cos \beta_k z.$$

Matching conditions at $\eta = 0$ are used to determine the unknown coefficients a_k and b_k

from

$$\left.\begin{aligned} \phi_w = \phi_c + \phi_s = \quad & \phi_c + \sum a_k \cos\beta_K z \\ 0 = u_c + u_s = \quad & u_c - \sum \underbrace{Ha^{1/2}\alpha_k\,(b_k + a_k)}_{u_k} \cos\beta_k z \end{aligned}\right\} \text{ at } \eta = 0. \tag{38}$$

The coefficients a_k and u_k correspond to the Fourier coefficients of viscous potential and velocity taken at the position $y = 1$ (at $\eta = 0$). While the core values are independent of the field aligned coordinate according to (22) and (23), the value ϕ_w, known from the numerical solution depends on z.

We find by using orthogonality of trigonometric functions the equations determining the a_k and u_k as

$$a_k = \frac{2}{Z}\int_0^Z (\phi_w - \phi_c)\cos\beta_k z\, dz, \tag{39}$$

$$u_k = \frac{2}{Z}\int_0^Z u_c \cos\beta_k z\, dz, \tag{40}$$

which determine the last coefficient

$$b_k = -a_k + \frac{1}{\alpha_k Ha^{1/2}} u_k$$

for the side layer velocity in (37). The analysis follows the ideas of Walker (1981) who calculated the coefficients up to the leading order in *Ha*.

We have seen in (23) that the core velocity u_c is uniform along magnetic field lines. This simplifies the calculation for u_k and we obtain

$$u_k = 2u_c \frac{\sin Z\beta_k}{Z\beta_k}. \tag{41}$$

The core potential ϕ_c is constant along field lines but the potential difference $(\phi_w - \phi_c)$ depends on z. The values $(\phi_w - \phi_c)$ are known at discrete locations as a result from the numerical calculations. For evaluating the expression (39) we assume that for the simplest case the potential varies like a piecewise linear function between the numerically known values at the ends of a line element l. This yields

$$a_k = \frac{2}{Z\beta_k^2} \sum_{l=1}^{n} [\phi_w - \phi_c]_l \frac{[\cos\beta_k z]_l}{[z]_l}, \tag{42}$$

where $[\ ]_l$ stands for the difference of a quantity taken between the two nodes of the line element l. The summation over all n line elements gives the value of the integral (39).

Results for velocity profiles at different axial positions for the case of a sudden expansion are shown in Figs. 12-15 for $Ha = 10^3$. Far downstream and upstream of the expansion we observe the typical velocity profiles of fully established rectangular duct flows with a flat uniform core and high-velocity jets along the side walls. Approaching the expansion the core becomes deformed and we observe the inviscid (outer) layers which are much thicker than the viscous sub layers. Within the inviscid layers the velocity is

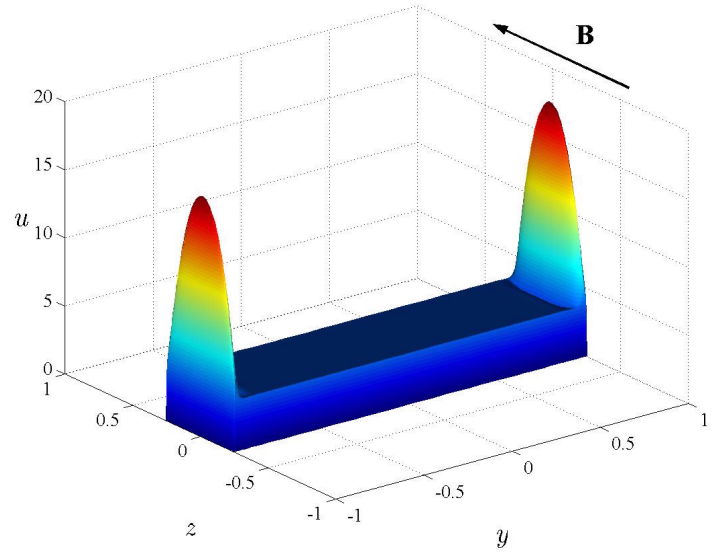

Figure 12: Fully developed velocity profile far upstream of the expansion

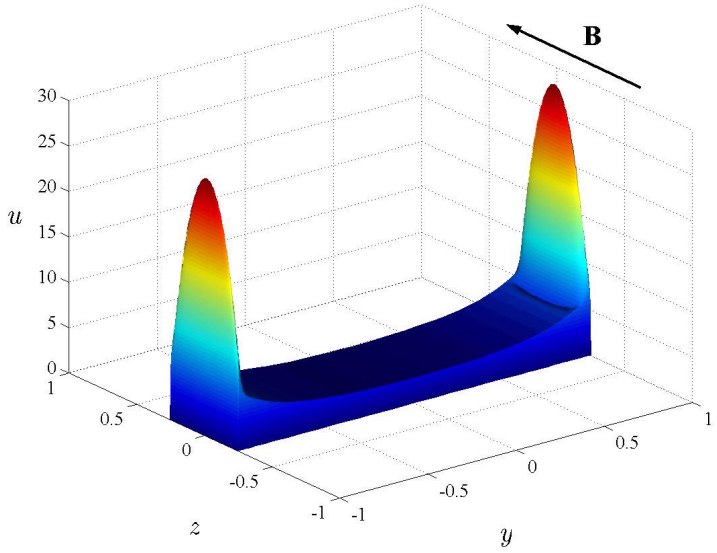

Figure 13: Velocity profile immediately in front of the expansion at $x = -0.1$

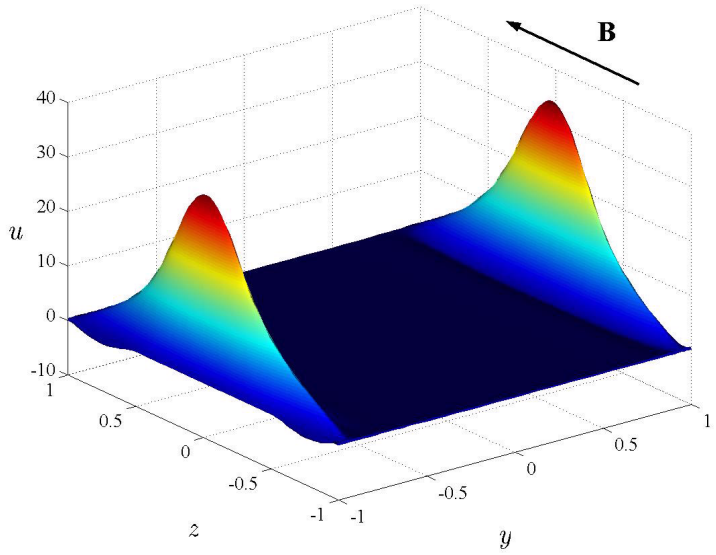

Figure 14: Velocity profile immediately behind the expansion at $x = 0.1$

already increased. In addition the flux carried by the viscous side layer increases also due to the exchange of flow with the core. This leads to the high velocities in the side layers which can be observed near the expansion in Fig. 13. Immediately behind the expansion, as shown in Fig. 14, the major fraction of the flow is carried by the side layers, which have received from the flow upstream the expansion and from the expansion layer about 80% of the total flux. The velocity profile along field lines is no longer parabolic as known for fully established flows. There exists even a reversed flow closer to the corners of the duct. The back flow disappears downstream after some length and the fluid finally approaches fully developed conditions at the exit of the computational domain as shown in Fig. 15

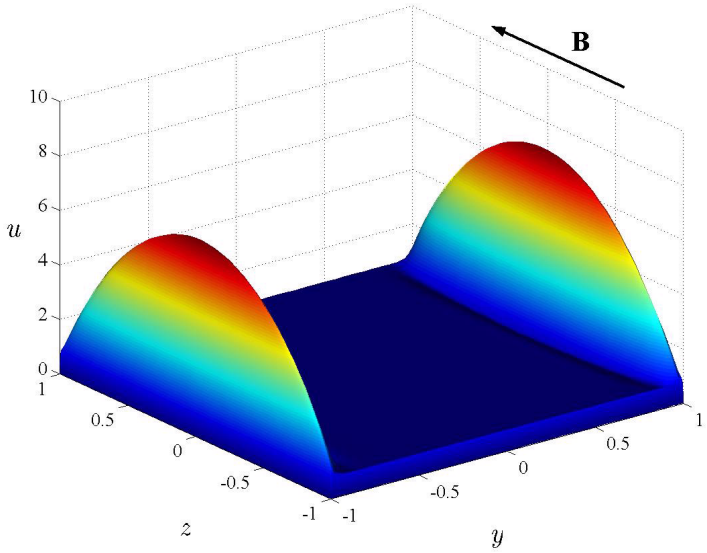

Figure 15: Fully developed velocity profile far downstream of the expansion

4.3 Expansion layer

Expansion layers occur if $L_{\exp} \lesssim Ha^{-1/2}$ as it is the case for a sudden expansion. In the analysis we use the same ideas as for the solution of the side layer problem. Let us suppose that an inviscid solution to the problem is known, i.e. we know core potentials and velocities at both sides of a sudden expansion and the wall potential at the expansion.

4.3.1 Potential and transverse flow

We introduce a stretched coordinate in (16) for the expansion layer such that

$$x = \delta_e \xi, \tag{43}$$

where δ_e stands for the thickness of the expansion layer. A reasonable balance of viscous and Lorentz forces requires that $\delta_e = Ha^{-1/2}$ and we find at leading order of our analysis the equation governing the potential in the expansion layer,

$$\partial_\xi^4 \phi = \partial_{zz} \phi. \tag{44}$$

The transverse velocity in the plane of the layer is related at this order of approximation to the potential as

$$v = Ha^{1/2} \partial_\xi \phi. \tag{45}$$

The separable partial differential equation (44) is solved on the domain shown in Fig. 16, assuming symmetry with respect to $z = 0$. As already discussed for the side layers, the thin wall condition (**??**) formulated in stretched coordinates results in a uniform potential along the stretched direction, i.e. the Hartmann walls act here as a perfect conductors along the axial direction if $c\,Ha \gg 1$. For that reason the potential equals the core potential at the Hartmann wall and the viscous corrections vanish at the Hartmann walls. As $\xi \to \pm\infty$ the solution must match the core solution which is equivalent with the requirement that viscous corrections to the core potential and velocity vanish as $\xi \to \pm\infty$. In addition the potential along the vertical wall must equal the wall potential and the velocity must vanish along this wall at $\xi = 0$. For the solution we split the domain into two parts, one for $\xi < 0$, in which the duct has a dimension along magnetic field lines up to $Z = Z_c$ and a second part for $\xi \geq 0$ where $Z = Z_C = 1$.

Let us start the analysis for $\xi \geq 0$. We decompose the potential as $\phi = \phi_C + \phi_E$, into an inviscid core solution ϕ_C and into a viscous correction ϕ_E. Similarly we decompose the velocity as $v = v_C + v_E$, where v_C and v_E stand for the core velocity and the viscous correction in the expansion layer.

Equation (44) has the z- symmetric solution that does not grow indefinitely as $\xi \to \infty$:

$$\phi_E = \sum_{K=0}^{\infty} \left(A_K \cos \alpha_K \xi + B_K \sin \alpha_K \xi\right) \exp \alpha_K \xi \, \cos \beta_K z, \tag{46}$$

where

$$\beta_K = \frac{2K+1}{2} \frac{\pi}{Z_C}, \quad \alpha_K = -\sqrt{\beta_K/2}. \tag{47}$$

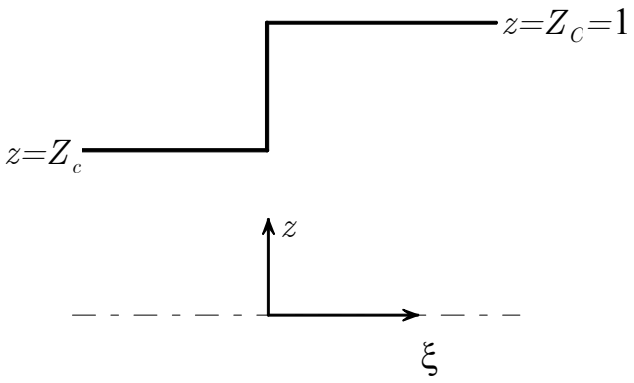

Figure 16: Coordinates and geometry in the upper half expansion layer

The velocity evaluates as

$$\begin{aligned} v_E &= Ha^{1/2}\partial_\xi \phi_E \\ &= \sum Ha^{1/2}\alpha_K \left[(B_K + A_K)\cos\alpha_K\xi + (B_K - A_K)\sin\alpha_K\xi\right]\exp\alpha_K\xi\ \cos\beta_K z. \end{aligned} \tag{48}$$

Matching conditions at $\xi = 0$ are later used to determine the unknown coefficients A_K and B_K from

$$\left.\begin{aligned} \phi = \phi_C + \phi_E = &\quad \phi_C + \sum A_K \cos\beta_K z \\ v = v_C + v_E = &\quad v_C + \sum \underbrace{Ha^{1/2}\alpha_K\,(B_K + A_K)}_{V_K}\cos\beta_K z \end{aligned}\right\} \text{ at } \xi = 0 \tag{49}$$

The coefficients A_K and V_K correspond to the Fourier coefficients of viscous potential and velocity taken at the position $\xi = 0$. While the core values are independent of the field aligned coordinate according to (22) and (23), the values ϕ and v at $\xi = 0$ do depend on z.

For $\xi < 0$ we perform a similar analysis and decompose the electric potential as $\phi = \phi_c + \phi_e$, into an inviscid core solution ϕ_c and into a viscous correction ϕ_e. Similarly we decompose the velocity as $v = v_c + v_e$, where v_c and v_e stand for the core velocity and the viscous correction in the expansion layer for $\xi < 0$. In this part of the geometry the extension of the duct along field lines is between $-Z_c < z < Z_c$.

Equation (44) has the solution that does not grow indefinitely as $\xi \to -\infty$, i.e.

$$\phi_e = \sum_{k=0}^{\infty} (a_k \cos\alpha_k\xi + b_k \sin\alpha_k\xi)\exp\alpha_k\xi\ \cos\beta_k z, \tag{50}$$

where

$$\beta_k = \frac{2k+1}{2}\frac{\pi}{Z_c}, \quad \alpha_k = +\sqrt{\beta_k/2}. \tag{51}$$

The velocity here is given by

$$\begin{aligned} v_e &= Ha^{1/2}\partial_\xi \phi_e \\ &= \sum Ha^{1/2}\alpha_k \left[(a_k + b_k)\cos\alpha_k\xi + (b_k - a_k)\sin\alpha_k\xi\right]\exp\alpha_k\xi\ \cos\beta_k z. \end{aligned} \tag{52}$$

Matching conditions at $\xi = 0$ couple the coefficients a_k and b_k with the values of potential and velocity as

$$\left.\begin{aligned} \phi = \phi_c + \phi_e = \quad & \phi_c + \textstyle\sum a_k \cos\beta_k z \\ v = v_c + v_e = \quad & v_c + \textstyle\sum \underbrace{Ha^{1/2}\alpha_k\,(a_k + b_k)}_{v_k} \cos\beta_k z \end{aligned}\right\} \quad \text{at } \xi = 0\,. \tag{53}$$

Elimination of ϕ and v at $\xi = 0$ from (49) and (53) yields

$$\phi_C + \sum_K A_K \cos\beta_K z = \begin{cases} \phi_w & \text{for } Z_c < z < Z_C \\ \phi_c + \sum_k a_k \cos\beta_k z & \text{for } 0 < \ z \le Z_c \end{cases}, \tag{54}$$

$$v_C + \sum_K V_K \cos\beta_K z = \begin{cases} 0 & \text{for } Z_c < z < Z_C \\ v_c + \sum_k v_k \cos\beta_k z & \text{for } 0 < \ z \le Z_c \end{cases}. \tag{55}$$

The potential and the velocity at $\xi = 0$ are given by the expressions shown in (53) for $0 < z \le Z_c$. For $Z_c < z < Z_C$, however, the potential $\phi\,(\xi = 0)$ equals the wall potential ϕ_w and the velocity at the solid wall vanishes. We find by using orthogonality of trigonometric functions and with the abbreviations

$$\Delta\phi = \begin{cases} \phi_w - \phi_C \\ \phi_c - \phi_C \end{cases} \quad \text{and} \quad \Delta v = \begin{cases} 0 - v_C & \text{for } Z_c < z < Z_C \\ v_c - v_C & \text{for } 0 < \ z \le Z_c \end{cases} \tag{56}$$

the equations determining the A_K and B_K as

$$\frac{1}{2}A_K = \frac{1}{Z_C}\left(\sum_k a_k \int_0^{Z_c} \cos\beta_k z \cos\beta_K z\,dz + \int_0^{Z_C} \Delta\phi \cos\beta_K z\,dz\right), \tag{57}$$

$$\frac{1}{2}V_K = \frac{1}{Z_C}\left(\sum_k v_k \int_0^{Z_c} \cos\beta_k z \cos\beta_K z\,dz + \int_0^{Z_C} \Delta v \cos\beta_K z\,dz\right). \tag{58}$$

So far the coefficients A_K and V_K (B_K) satisfy continuity of potential and velocity at $\xi = 0$ for any given expansion of the solution in terms of a_k and v_k (b_k).

Continuity of shear stress (vorticity) at $\xi = 0$ is used now to derive equations for a_k and b_k, i.e.

$$\partial_{\xi\xi}\phi_e\,(\xi = -0) = \partial_{\xi\xi}\phi_E\,(\xi = +0)\,. \tag{59}$$

We obtain now

$$\sum_k \alpha_k^2 b_k \cos\beta_k z = \sum_K \alpha_K^2 B_K \cos\beta_K z, \tag{60}$$

and after using orthogonality we find

$$\frac{1}{2}Z_c\alpha_k^2 b_k = \sum_K B_K \alpha_K^2 \int_0^{Z_c} \cos\beta_K z \cos\beta_k z\,dz. \tag{61}$$

If we further assume that the vorticity field is smooth at $\xi = 0$,

$$\partial_\xi^3 \phi_e \left(\xi = -0\right) = \partial_\xi^3 \phi_E \left(\xi = +0\right), \tag{62}$$

we find the equation

$$\sum_k \alpha_k^3 \left(b_k - a_k\right) \cos \beta_k z = \sum_K \alpha_K^3 \left(B_K - A_K\right) \cos \beta_K z, \tag{63}$$

from which we determine

$$\frac{1}{2} Z_c \alpha_k^3 \left(b_k - a_k\right) = \sum_K \left(B_K - A_K\right) \alpha_K^3 \int_0^{Z_c} \cos \beta_K z \cos \beta_k z \, dz. \tag{64}$$

In the next step we substitute the integrals as

$$C_{kK} = 2 \int_0^{Z_c} \cos \beta_K z \cos \beta_k z \, dz = 2 \frac{\beta_k \cos Z_c \beta_K \sin Z_c \beta_k}{\beta_k^2 - \beta_K^2}, \tag{65}$$

$$\Delta\phi_K = \frac{2}{Z_C} \int_0^{Z_C} \Delta\phi \cos \beta_K z \, dz, \quad \Delta v_K = \frac{2}{Z_C} \int_0^{Z_C} \Delta v \cos \beta_K z \, dz. \tag{66}$$

Note, there is a possibility that the denominator in (65) vanishes if $\beta_K \to \beta_k$. For such a case it can be shown, however, that C_{kK} remains finite:

$$\lim_{\beta_K \to \beta_k} C_{kK} = Z_c. \tag{67}$$

The core velocities are uniform along field lines so that Δv becomes a piecewise constant function along z. The Fourier coefficients evaluate analytically as

$$\begin{aligned} \Delta v_K &= \frac{2}{Z_C} \left(\int_0^{Z_c} \left(v_c - v_C\right) \cos \beta_K z \, dz + \int_{Z_c}^{Z_C} \left(-v_C\right) \cos \beta_K z \, dz \right) \\ &= \frac{2}{Z_C \beta_K} \left(v_c \sin \beta_K Z_c - v_C \sin \beta_K Z_C\right). \end{aligned} \tag{68}$$

The values v_c and v_C have to be taken from the numerical solution. The function $\Delta\phi\left(z\right)$ is not known analytically but may be approximated in the simplest case as a continuous piecewise linear function that connects the numerically obtained potential data. Analytic integration of the piecewise function yields

$$\Delta\phi_K = \frac{2}{\beta_K^2 Z_C} \sum_{l=1}^{n} \left[\Delta\phi\right]_l \frac{\left[\cos \beta_K Z\right]_l}{\left[Z\right]_l}, \tag{69}$$

where $\left[\ \right]_l$ stands for the difference of a quantity taken between two nodes of the computational grid. This procedure ensures convergence as $K \to \infty$ in contrast to an approximation that would take $\Delta\phi$ at a finite number of collocation points.

The final system of equations that determines the solution of the flow in the expansion layer reads as

$$A_K = \frac{1}{Z_C}\sum_k a_k C_{kK} + \Delta\phi_K, \tag{70}$$

$$V_K = \frac{1}{Z_C}\sum_k v_k C_{kK} + \Delta v_K. \tag{71}$$

With $v_k = Ha^{1/2}\alpha_k\,(a_k + b_k)$ and and $B_K = -A_K + \frac{V_K}{\alpha_K Ha^{1/2}}$ the latter equation determines B_K as

$$B_K = -A_K + \frac{1}{Z_C}\frac{1}{\alpha_K}\sum_k \alpha_k\,(a_k + b_k)\,C_{kK} + \frac{1}{\alpha_K Ha^{1/2}}\Delta v_K.$$

The system of equations is finally closed by the determination of the coefficients a_k and b_k. We summarize the governing equations as follows:

$$A_K = \frac{1}{Z_C}\sum_k a_k C_{kK} + \Delta\phi_K \tag{72}$$

$$B_K = -A_K + \frac{1}{Z_C\alpha_K}\sum_k \alpha_k\,(a_k + b_k)\,C_{kK} + \frac{1}{\alpha_K Ha^{1/2}}\Delta v_K \tag{73}$$

$$b_k = \frac{1}{Z_c\alpha_k^2}\sum_K \alpha_K^2 B_K C_{kK}, \tag{74}$$

$$a_k = b_k - \frac{1}{Z_c\alpha_k^3}\sum_K \alpha_K^3\,(B_K - A_K)\,C_{kK}. \tag{75}$$

We see already that the problem is mainly governed by core potentials and that the corrections due to core velocity become unimportant as $Ha \to \infty$. For a numerical solution of the problem the series are truncated at a finite number of modes and the solution is obtained by an iterative process. Initially $a_k = b_k = 0$ is assumed and first estimates of A_K and B_K are calculated. Then b_k and a_k are updated and a better approximation for A_K and B_K is obtained. This procedure is repeated (with underrelaxation if necessary) until A_K, B_K and a_k, b_k approach their final constant values.

As a result, isolines of transverse velocity are plotted in Fig. 2 for the expansion layer at a position close to the side wall near $y = 1$. The Hartmann number is $Ha = 1000$ for the present case. Far upstream the transverse velocity is equal to v_c. The Hartmann layers are so thin that they are not visible in the graph. Approaching the expansion we observe a weak local minimum of the transverse velocity near $\xi \approx -1.5$. Then, the velocity increases strongly along the axis and the maximum is reached near $\xi \approx 0.7$. Later the velocity decays and approaches via a local minimum, not visible in the figure, the core value v_C. The profile of transverse velocity plotted along the duct axis is shown in Fig. 18.

The most interesting thing is that the maximum of the e− layer velocity is not located on the axis at $z = 0$, as one could have expected. Instead we observe two maxima close to the positions $z \approx \pm Z_c$ which are obviously a result of the corner singularities at the expansion. While the major fraction of the flow in the layer is carried towards the sides,

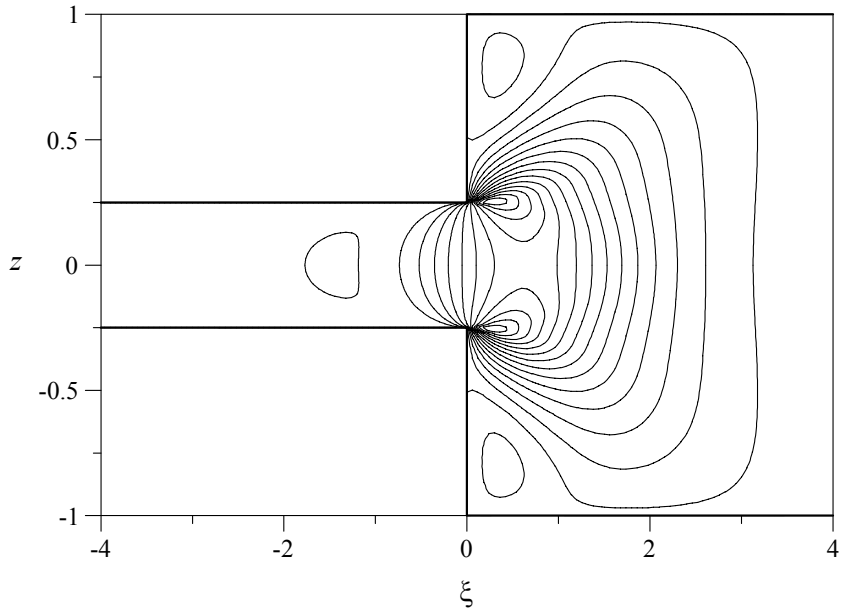

Figure 17: Contour plot of transverse velocity v in the e-layer close to the side wall $y \lesssim 1$ for $Ha = 1000$.

the solution exhibits also regions closer to the outer corners, in which the direction of velocity is reversed. In these regions fluid is sucked from the side layer and transferred towards the center of the duct. The two maxima and the reversed flow are visible in Fig. 19. These findings are consistent with the axial velocity profile behind the expansion as shown in Fig. 14, where near the corners zones of reversed flow are also present.

To continue the analysis we consider integral quantities of the layer and compare them with the solutions in the cores. Since in general the inviscid axial mass flux is discontinuous across the expansion layer, the layer must carry an $O(1)$ flow rate transverse to the axis towards the sides. If we are interested in the amount of flow carried by the layer at position y we may integrate the velocity profile and find the local flow rate

$$q_y(y,z) = Ha^{-1/2}\left(\int_{-\infty}^{0} v_e\, d\xi + \int_{0}^{\infty} v_E\, d\xi\right) = -\Delta\phi\,.$$

The amount of fluid carried through an entire cross section of the e- layer at position y evaluates from the latter quantity as

$$Q_e(y) = \int_0^{Z_C} q_y\, dz = -\int_0^{Z_C} \Delta\phi\; dz. \tag{76}$$

This means that the flow rate is determined by the difference between the core potential in the large duct and the potential along the vertical wall and in the small core. It is possible to compare the potential-driven transverse flow rate with the fluxes calculated by the numerical code, i.e. $Q_e = \psi_C - \psi_c$. A comparison shows that the difference between both quantities is

$$\psi_C - \psi_c + \int_0^{Z_C} \Delta\phi\; dz = 0 + \varepsilon_{\mathrm{num}}, \tag{77}$$

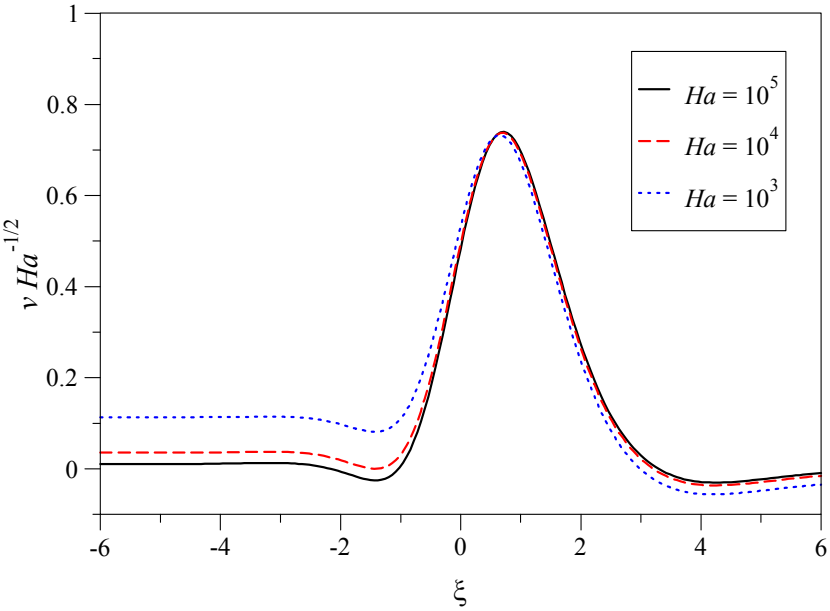

Figure 18: Transverse velocity v along the axis of the duct for $z = 0$, $y \lesssim 1$

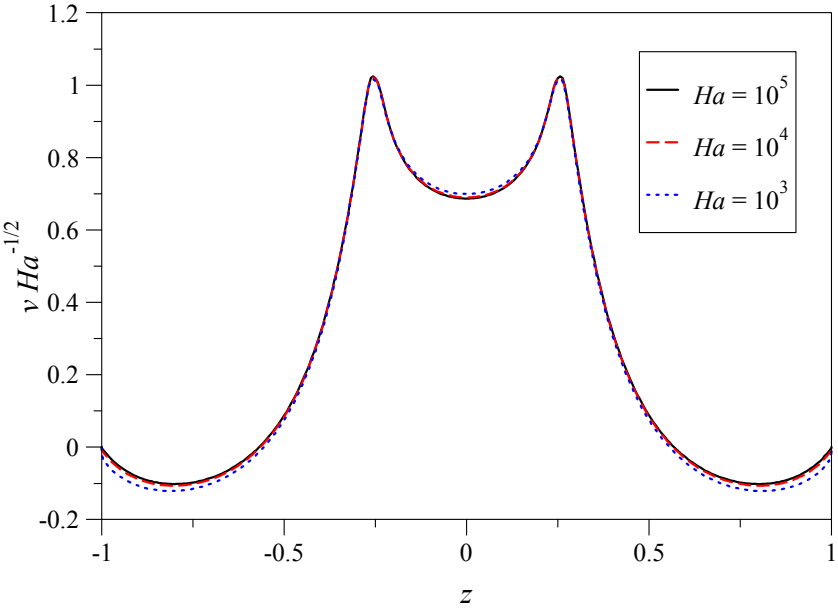

Figure 19: Transverse velocity v along magnetic field lines for $\xi = 0.4$, $y \lesssim 1$

which is as small as the numerical error of the current approximation, $\varepsilon_{\rm num} \lesssim 10^{-2}$.

4.3.2 Vertical flow

For deriving an equation for vertical velocity in the expansion layer we use (20) in stretched coordinates as

$$\partial_\xi^4 w = \partial_{zz} w. \tag{78}$$

At large distance from the expansion the solution for w requires that

$$w = \partial_\xi w = 0 \text{ as } \xi \to \pm\infty. \tag{79}$$

The boundary conditions at Hartmann walls are

$$w = 0 \text{ at } z = Z_{c,C} \tag{80}$$

and symmetry implies that

$$w = 0 \text{ at } z = 0. \tag{81}$$

At the vertical wall of the expansion, for $Z_c < z < Z_C$, we have no-slip and zero normal component of velocity,

$$w = 0 \;\text{ and }\; u = 0 \text{ at } \xi = 0. \tag{82}$$

In general, the axial component u of velocity evaluates at leading order from Ohm's law as

$$u = -\partial_x p - \partial_y \phi. \tag{83}$$

The variables and expressions for u, $\partial_x p$, and $\partial_y \phi$ are used for continuous matching at $\xi = 0$ for $0 < z < Z_c$.

As before we split the expansion domain in two regions and define the vertical velocity as

$$w = \begin{cases} Ha^{1/2} w_e & \xi < 0 \\ \qquad\quad \text{for} & \\ Ha^{1/2} w_E & \xi > 0 \;\; . \end{cases} \tag{84}$$

By separation of variables we find viscous solutions for w, which vanish at large distance from the expansion in the form

$$w_E = \sum_{K=1}^{\infty} (A_K \cos\alpha_K \xi + B_K \sin\alpha_K \xi) \exp\alpha_K \xi \, \sin\beta_K z, \tag{85}$$

$$w_e = \sum_{k=1}^{\infty} (a_k \cos\alpha_k \xi + b_k \sin\alpha_k \xi) \exp\alpha_k \xi \, \sin\beta_k z, \tag{86}$$

where

$$\begin{array}{lll} \beta_K = \frac{1}{Z_C} K\pi, & \alpha_K = -\sqrt{\beta_K/2}, \\ \beta_k = \frac{1}{Z_c} k\pi, & \alpha_k = \sqrt{\beta_k/2}. \end{array} \tag{87}$$

At $\xi = 0$ we smoothly match both solutions up to the second derivatives:

$$\sum_K A_K \, \sin\beta_K z = \begin{cases} 0 & \text{for } Z_c < z < Z_C \\ \sum_k a_k \, \sin\beta_k z & \text{for } 0 < z < Z_c \end{cases} , \tag{88}$$

$$\sum_K \alpha_K \ (B_K + A_K) \sin \beta_K z = \sum_k \alpha_k \ (b_k + a_k) \sin \beta_k z \text{ for } 0 < z < Z_c, \tag{89}$$

$$\sum_K \alpha_K{}^2 B_K \sin \beta_K z = \sum_k \alpha_k^2 \, b_k \sin \beta_k z \text{ for } 0 < z < Z_c \ . \tag{90}$$

The fourth condition for matching is obtained by consideration of vertical fluxes as described below. The vertical component of velocity is related to pressure according to (17) at leading order as

$$\partial_{xx} p = \partial_z w \tag{91}$$

Integration along x yields the variation with z of the flow rate carried by the layer in the vertical direction, i.e.

$$\partial_x p_C - \partial_x p_{0+} = \int_0^\infty \partial_z w_E d\xi, \tag{92}$$

$$\partial_x p_{0-} - \partial_x p_c = \int_{-\infty}^0 \partial_z w_e d\xi, \tag{93}$$

where $\partial_x p_{0\pm} = \partial_x p \left(\xi = 0\pm\right)$ are the left and right sided limits of pressure gradient. Matching of pressure gradients (potential and velocity) at $\xi = 0$ leads us to

$$\int_0^\infty \partial_z w_E d\xi = G\left(z\right) - \left\{ \begin{array}{cc} 0 & Z_c < z < Z_C \\ \text{for} & \\ \int_{-\infty}^0 \partial_z w_e d\xi & 0 < z < Z_c \end{array} \right. , \tag{94}$$

where

$$G\left(z\right) = \left\{ \begin{array}{cc} \partial_x p_C - \partial_x p_{0+} & Z_c < z < Z_C \\ \text{for} & \\ \partial_x p_C - \partial_x p_c & 0 < z < Z_c \end{array} \right. . \tag{95}$$

Integration of (94) along z yields

$$\int_0^\infty w_E d\xi = \int_0^z G\left(z\right) dz - \left\{ \begin{array}{cc} 0 & Z_c < z < Z_C \\ \int_{-\infty}^0 w_e d\xi \ \text{ for } & 0 < z < Z_c \end{array} \right. . \tag{96}$$

Inserting the ansatz for w_E and w_e gives

$$\frac{1}{2} \sum_K \frac{B_K - A_K}{\alpha_K} \sin \beta_K z = \int_0^z G\left(z\right) dz + \left\{ \begin{array}{cc} 0 & Z_c < z < Z_C \\ \frac{1}{2} \sum_k \frac{b_k - a_k}{\alpha_k} \sin \beta_k z \ \text{ for } & 0 < z < Z_c \end{array} \right. \tag{97}$$

and orthogonality determines the coefficients as

$$\frac{B_K - A_K}{\alpha_K} = \frac{4}{Z_C} \int_0^{Z_C} \left(\int_0^z G\left(z'\right) dz' \sin \beta_K z \right) \, dz + \frac{1}{Z_C} \sum_k \frac{b_k - a_k}{\alpha_k} S_{kK}, \tag{98}$$

with the abbreviation

$$S_{kK} = 2 \int_0^{Z_c} \sin \beta_k z \sin \beta_K z \, dz = \frac{2 \beta_k}{\beta_K^2 - \beta_k^2} \cos Z_c \beta_k \sin \beta_K Z_c. \tag{99}$$

The integral

$$G_K = \int_0^{Z_C} \left(\int_0^z G\left(z'\right) dz' \sin \beta_K z \right) dz \tag{100}$$

can be evaluated using integration by parts as

$$G_K = \frac{1}{\beta_K} \left(\int_0^{Z_C} G\left(z\right) \cos \beta_K z dz - \cos \beta_K Z_C \int_0^{Z_C} G\left(z\right) dz \right). \tag{101}$$

We shall show now that the second integral vanishes identically, i.e. $\int_0^{Z_C} G\left(z\right) dz = 0$ at the present order of approximation. This is immediately shown by integration of (94) along z. In order to demonstrate the consistency of the current models we show the same fact once more. For this purpose let us consider (95), in which we substitute the pressure gradient according to $\partial_x p = -\left(u + \partial_y \phi\right)$, i.e.

$$G\left(z\right) = \begin{cases} 0 - u_C & +\partial_y \left(\phi_w - \phi_C\right) \\ & \text{for} \\ u_c - u_C & +\partial_y \left(\phi_c - \phi_C\right) \end{cases} \begin{array}{c} Z_c < z < Z_C \\ \\ 0 < z < Z_c \end{array}. \tag{102}$$

We integrate this quantity along z and obtain

$$\int_0^{Z_C} G\left(z\right) dz = -\left(u_C Z_C - u_c Z_c + \partial_y Q_e\right), \tag{103}$$

where $Q_e = -\int_0^{Z_C} \Delta\phi \; dz$ according to (76) has been used. This equation states that the difference in axial fluxes through a volume element of transverse size dy changes the fluxes Q_e in the transverse direction. Therefore, conservation of mass requires that

$$\int_0^{Z_C} G\left(z\right) dz = 0. \tag{104}$$

For efficient computations we evaluate the velocity in G by the use of the 2D streamfunction as $u_{c,C} = -\frac{1}{Z_{c,C}} \partial_y \psi_{c,C}$ and find

$$G\left(z\right) = \partial_y \begin{cases} \frac{1}{Z_C}\psi_C & +\phi_w - \phi_C \\ & \text{for} \\ \frac{1}{Z_C}\psi_C - \frac{1}{Z_c}\psi_c & +\phi_c - \phi_C \end{cases} \begin{array}{c} Z_c < z < Z_C \\ \\ 0 < z < Z_c \end{array}. \tag{105}$$

In terms of the streamfunction the integral shown above reads as (compare with (77))

$$\int_0^{Z_C} G\left(z\right) dz = \partial_y \left(\psi_C - \psi_c + \int_0^{Z_C} \Delta\phi \; dz \right) = 0 + \partial_y \varepsilon_{\text{num}} \tag{106}$$

For this reason we can calculate G_K only from the first integral in (101). With orthogonality used through (88)-(90) we arrive at the final set of equations determining the

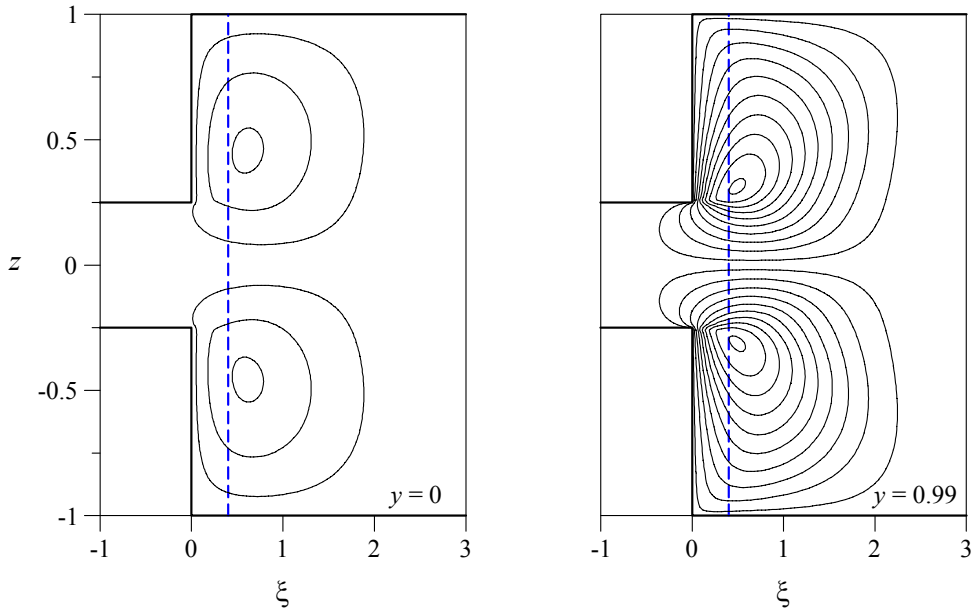

Figure 20: Contour plots of vertical velocity w in the e-layer at $y = 0$ and close to the side wall

vertical component w of velocity as

$$A_K = \frac{1}{Z_C} \sum_k a_k S_{kK}, \tag{107}$$

$$B_K - A_K = \frac{\alpha_K}{Z_C} \sum_k \frac{b_k - a_k}{\alpha_k} S_{kK} + \frac{4\alpha_K}{Z_C} G_K, \tag{108}$$

$$b_k = \frac{1}{\alpha_k^2 Z_c} \sum_K {\alpha_K}^2 B_K S_{kK}, \tag{109}$$

$$b_k + a_k = \frac{1}{\alpha_k Z_c} \sum_K \alpha_K \left(B_K + A_K\right) S_{kK}. \tag{110}$$

Results are shown in Figs. 20, 21. At all walls $w = 0$ is satisfied. At $y = 0$ the highest vertical velocities occur near $\xi \approx 0.62$, $z \approx 0.45$. Approaching the side wall the vertical velocity increases in magnitude. This is a result of the fact that the flow coming from the small duct has to be distributed both to the internal layer (in the transverse direction) and to the large core. The flow rate supplied to the expansion layer by the small core increases towards the sides as was shown already in Fig. 13 and therefore the magnitude of vertical velocity increases also. In addition the flow rate carried by the layer increases also towards the sides which leads additionally to higher velocities in the layer. We observe also that the location of maximum vertical velocity shifts to positions closer to the expansion, i.e. to $\xi \approx 0.45$, $z \approx 0.3$.

Profiles of vertical velocity at $\xi = 0.4$ (indicated by the dashed line in the previous figure) are displayed in Fig. 21 for different transverse positions in the duct. The vertical component of velocity scales as $Ha^{1/2}$ and takes maximum values of magnitude as $w \sim$

$0.14Ha^{1/2}$ for $y = 0$ up to values such as $w \sim 0.5Ha^{1/2}$ at a position close to the side wall.

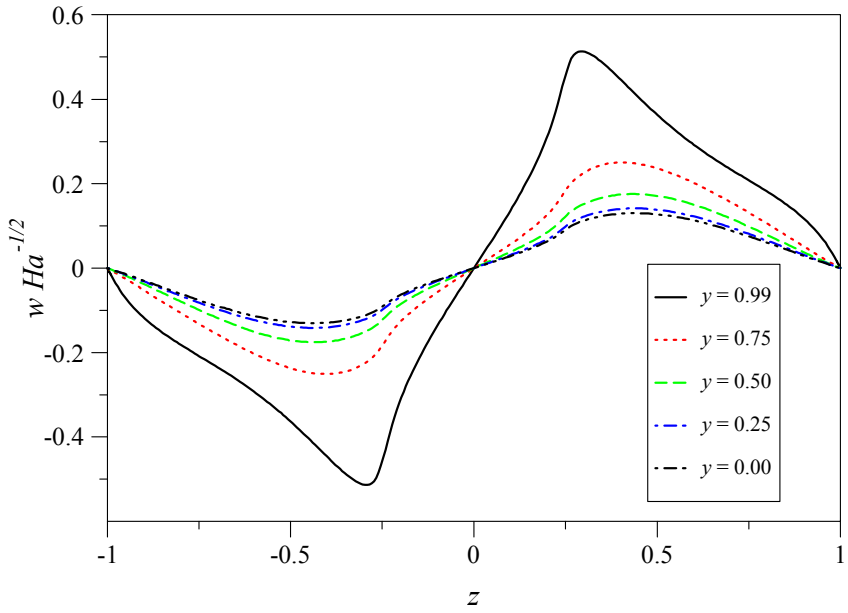

Figure 21: Vertical velocity w plotted along z for $\xi = 0.4$

From the results obtained above we may evaluate the local vertical flow rate as

$$q_z(y,z) = \int_{-\infty}^{\infty} w d\xi = \int_0^z G(z)\, dz. \tag{111}$$

4.3.3 Mass flux along the layer

In order to get an overview how the flux carried by the e- layer is distributed we plot the two-dimensional vector field q_y, q_z in the plane of the expansion layer. It can be seen that all the net flow which is collected by the layer is distributes towards the sides of the duct. the highest fluxes appear near $z = \pm\frac{1}{2}$. Regions of reversed flux (flux from the side towards the center) are not present. This means that the reversed velocities observed in Fig. 19 are at least compensated by flows towards the sides so that there exists no reversed net flux carried by the layer.

4.3.4 Flow paths

In this section we describe the topology of the flow pattern in the e-layer. For simplicity we restrict the discussion to one quarter of the symmetric expansion as shown in Fig. 23. We have seen already in Fig. 7 that there is an intense exchange of flow between cores, side layers and the internal layer. Before reaching the internal layer the mass flux in the side layer increases because of an exchange between upstream core and upstream side layer. So when we approach the expansion the side layer carries already 13% of the total flow. This flow is transferred to the downstream side layer. Possible flow paths for this fraction of flow are shown as red lines in Fig. 23.

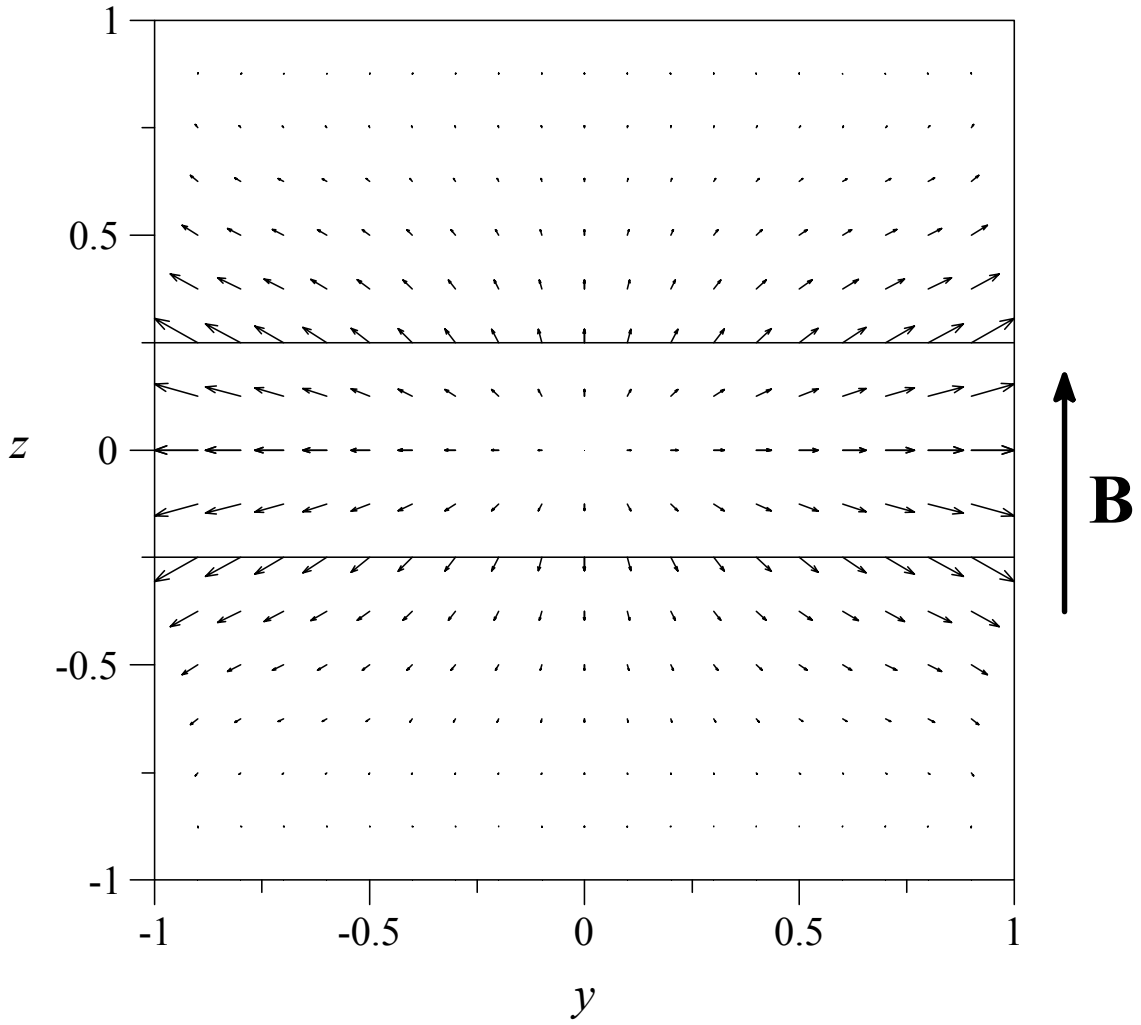

Figure 22: Vector plot of integral flux carried by the expansion layer

The streamlines shown in Fig. 7 indicate also that there exists a minor fraction of fluid (less than 20%) that is able to cross the internal layer from upstream to downstream core. One such path is indicated in Fig. 23 by the green line. The one shown here lies just in the symmetry plane. All other lines of this type (not shown here explicitly) are shifted upwards but also towards the sides during their path across the e-layer before they reach the downstream core.

A third type of streamline is shown in blue. Blue color indicates streamlines which start in the upstream core, enter the e- layer, and stay there until they meet the side layer. This part of flow continues its path though the downstream side layer. It has been shown above that behind the expansion region the downstream side layer carries about 80% of the flow.

The axial velocity profile just behind the e- layer, shown in Fig. 14, exhibits regions of reversed flow in the side layer close to the corners. The transverse velocity plotted in Fig. 17 shows also regions of locally reversed flow. A flow path consistent with these results is shown in magenta. For several reasons this seems to be the only possibility for a consistent flow pattern. One reason is that there is no reversed flux when integrated across the thickness of both the side layer and the e- layer. This means that the reversed velocity is at least compensated by an opposite flow in the same layer in horizontal planes. One could also think about a closure of streamlines in the layers in vertical planes. This, however, can be excluded because there is no downward vertical velocity component in the e- layer (compare Figs. 20 and 21). Moreover, closed streamlines in planes perpendicular to the magnetic field are often preferred in MHD flows because such flows minimize Joule damping. It should be noted that the magenta loop operates close to the walls and it is very likely that streamlines of the blue and green type exist just behind it.

Further downstream the side layer is rearranged. The downstream core sucks monotonically fluid from this layer until fully developed conditions establish.

5 Conclusions

MHD flows in geometries which expand along field lines have been investigated using asymptotic techniques valid for creeping flows in strong magnetic fields. For the analysis of such flows, inertia forces are neglected in comparison with Lorentz or pressure forces for $N \to \infty$. Viscous forces are confined to thin boundary layers or to thin internal parallel layers and they do not affect pressure drop or flow rates at leading order of the analysis for well conducting walls. The analysis shows that 3D effects disappear for very long expansions, when $L_{\rm exp} \gg 1$. With decreasing expansion length, 3D effects become gradually more important and the inviscid inertialess solution develops discontinuities in pressure gradient and side layer flow rates near the expansion as $L_{\rm exp} \to 0$. Approaching the expansion, the flow rate carried by the side layer increases. At the expansion, the side layers are fed additionally by the flow rate supplied from the expanding core. As $L_{\rm exp} \to 0$ there exists no expanding core any more and the geometry forms a sudden expansion. At the sudden expansion a viscous expansion layer appears transverse to the axis, which collects almost all flow from the upstream core and distributes it towards both sides. For the present case, about 80% of the total flow is now confined to the side

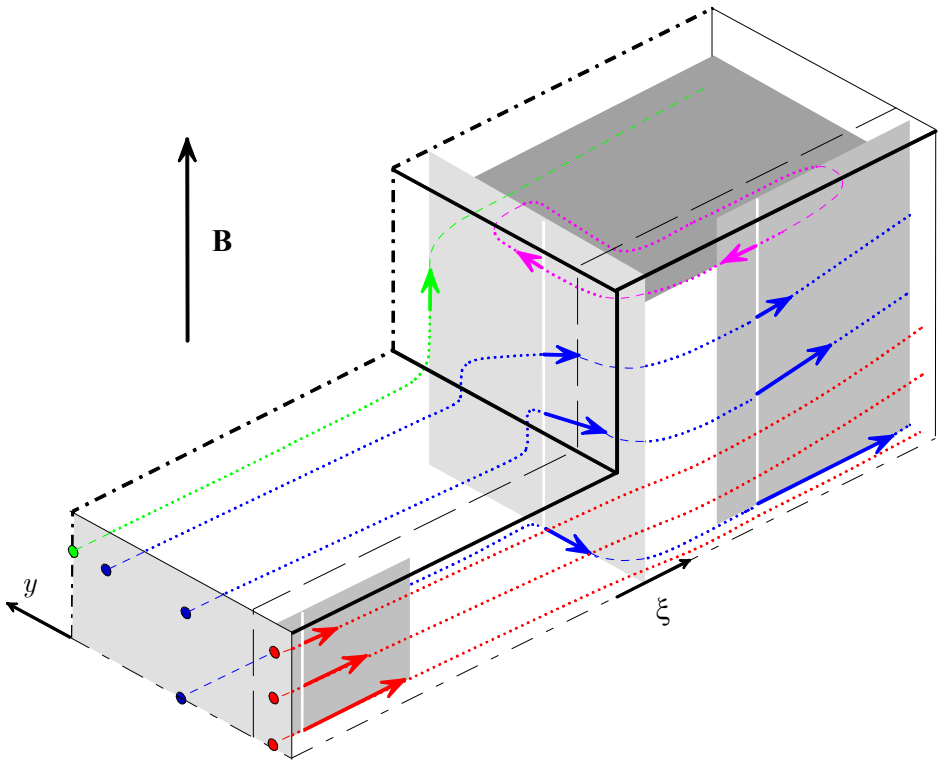

Figure 23: Flow paths in the e-layer. Red lines: flow stays within side layer; blue lines: flow from upstream core enters the e-layer and is transferred into the downstream side layer; green lines: flow from upstream core crosses the e-layer and enters downstream core; magenta lines: recirculation region involving downstream side layer and e-layer

layers from where it is redistributed downstream to the core.

Let us discuss finally some arguments about the validity of the inertialess approximation. It has been shown that the thickness of side layers scale as $Ha^{-1/2}$ and the expanding core has a length of $L_{\exp}$. Since both the side layers and the expanding core may carry an order one flow rate, the velocity may reach values up to the order $u \sim Ha^{1/2}$ and $v \sim L_{\exp}^{-1}$. Across the expanding core the axial velocity drop is of the order one on a length scale $L_{\exp}$ and we may estimate $u\partial_x u = O\left(L_{\exp}^{-1}\right)$. In the expanding core the fluid is accelerated transverse to the duct axis up to a velocity $v = O\left(L_{\exp}^{-1}\right)$ towards the sides, along a distance of order one. This yields transverse inertial forces $v\partial_y v = O\left(L_{\exp}^{-2}\right)$, which are even stronger than the axial components in the core. At the expansion, where most of the flow is collected in the side layer, the flow must be accelerated from velocities $u = O\left(Ha^{1/2}\right)$ to $3-4$ times this value along a distance $L_{\exp}$. This leads to inertia forces in the side layers of magnitude $u\partial_x u = O\left(L_{\exp}^{-1} Ha\right)$. It is expected that increasing inertia effects will firstly affect the flow in the side layers near the expansion, for high Hartmann numbers, i.e. for $L_{\exp} Ha > 1$. A further increase of inertia will then affect the flow in the expanding core and only very strong inertia forces may enter the axial momentum balance in the cores. As a result inertia is negligible if $N \gg L_{\exp}^{-1} Ha$. This relation should hold as long as the expansion length is large enough. For applications with sudden expansions the relevant length scale for axial changes has to be replaced by the thickness of the viscous internal layer $\delta_e \sim Ha^{-1/2}$. For such cases inertia becomes negligible only if $N \gg Ha^{3/2}$.

These simple considerations show already that the requirements on the interaction parameter are fairly strong in order that inertia effects remain negligible, i.e. $N \gg Ha^{3/2}$. Inertial flows in expansions, which are out of the scope of the present paper are currently investigated experimentally in the MEKKA laboratory of the Forschungszentrum Karlsruhe.

References

Branover, G. G., Vasil'ev, A. S. and Gel'fgat, Y. M.: 1967, Effect of a transverse magnetic field on the flow in a duct at a sudden cross section enlargement, *Magnitnaya Gidrodynamica* **3**(3), 61–65.

Bühler, L.: 1995, Magnetohydrodynamic flows in arbitrary geometries in strong, nonuniform magnetic fields, *Fusion Technology* **27**, 3–24.

Gel'fgat, Y. M. and Kit, L. G.: 1971, Investigation of the conditions of occurrence of M-shaped velocity profiles at sudden expansion or contraction of a magnetohydrodynamic flow, *Magnetohydrodynamics* **7**(1), 21–25.

Giancarli, L., Golfier, H., Nishio, S., Raffray, R., Wong, C. and Yamada, R.: 2002, Progress in blanket designs using SiCf/SiC composites, *Fusion Engineering and Design* **61-62**, 307–318.

Hunt, J. C. R. and Leibovich, S.: 1967, Magnetohydrodynamic flow in channels of variable cross-section with strong transverse magnetic fields, *Journal of Fluid Mechanics* **28**(Part 2), 241–260.

Molokov, S.: 1994, Liquid metal flows in manifolds and expansions of insulating rectangular ducts in the plane perpendicular to a strong magnetic field, *Technical Report KfK 5272*, Kernforschungszentrum Karlsruhe.

Molokov, S. and Bühler, L.: 1994, Liquid metal flow in a U-bend in a strong uniform magnetic field, *Journal of Fluid Mechanics* **267**, 325–352.

Moreau, R.: 1990, *Magnetohydrodynamics*, Kluwer Academic Publisher.

Picologlou, B. F., Reed, C. B., Hua, T. Q., Barleon, L., Kreuzinger, H. and Walker, J. S.: 1989, MHD flow tailoring in first wall coolant channels of self-cooled blankets, *Fusion Engineering and Design* **8**, 297–303.

Tillack, M. S. and McCarthy, K.: 1989, Flow quantity in side layers for MHD flow in conducting rectangular ducts, *Technical Report UCLA-IFNT-89-01*, University of California, Los Angeles.

Walker, J. S.: 1981, Magnetohydrodynamic flows in rectangular ducts with thin conducting walls, *Journal de Mécanique* **20**(1), 79–112.

Walker, J. S.: 1986, Laminar duct flows in strong magnetic fields, *in* H. Branover, P. S. Lycoudis and M. Mond (eds), *Liquid-metal flows and magnetohydrodynamics*, American Institute of Aeronautics and Astronautics.

Walker, J. S., Ludford, G. S. S. and Hunt, J. C. R.: 1972, Three-dimensional MHD duct flows with strong transverse magnetic fields. part 3. variable-area rectangular ducts with insulating walls, *Journal of Fluid Mechanics* **56**, 121–141.